## Author version

Published as:

van Schie, S. P., Ruh, M. L., Fletcher, A. H., Warner, M., Sperry, M., Scotzniovsky, L., Orndorff, N. C., Xiang, R., Yan, J., Zhao, H., Krokowski, J., Chen, J., Sarojini, D., Gill, H., Lee, S., Tagg, A. C., Anderson, R., Green, E., Joseph, C., Ning, A., Cheng, Z., Cao, Z., Mi, C., Guibert, A. T., Cronk, A., Kim, A. A., Meng, S., Silva, C., & Hwang, J. T. (2025). Large-scale distributed multidisciplinary design optimization of the NASA lift-plus-cruise air taxi concept. In AIAA SCITECH 2025 Forum (Paper No. AIAA 2025-0362). https://doi.org/10.2514/6.2025-0362

BibTeX for this reference:

https://lsdolab.github.io/lsdo-publications/publication/vanschie2025large/

```
@inproceedings{vanschie2025large,
  author = {Sebastiaan P. van Schie and Marius L. Ruh and Andrew H. Fletcher and Michael
    Warner and Mark Sperry and Luca Scotzniovsky and Nicholas C. Orndorff and Ru Xiang
    and Jiayao Yan and Han Zhao and Joshua Krokowski and Jiun-Shyan Chen and Darshan
    Sarojini and Hyunjune Gill and Seongkyu Lee and Andrew C. Tagg and Ryan Anderson and
    Eric Green and Cibin Joseph and Andrew Ning and Zeyu Cheng and Zhi Cao and Chunting
    Mi and Alexandre T. Guibert and Ashley Cronk and Alicia A. Kim and Shirley Meng and
    Christopher Silva and John T. Hwang},
  title = {Large-Scale Distributed Multidisciplinary Design Optimization of the NASA
    Lift-Plus-Cruise Air Taxi Concept},
  booktitle = {AIAA SCITECH 2025 Forum},
  year = {2025},
  doi = {10.2514/6.2025-0362},
  url = {https://doi.org/10.2514/6.2025-0362}
}
```

# Large-Scale Distributed Multidisciplinary Design Optimization of the NASA Lift-Plus-Cruise Air Taxi Concept

Sebastiaan P. C. van Schie, Marius L. Ruh, Andrew Fletcher, Michael Warner,
Mark Sperry, Luca Scotzniovsky, Nicholas C. Orndorff,
Ru Xiang, Jiayao Yan, Han Zhao, Joshua J. Krokowski[*],
J. S. Chen[†]
*University of California San Diego, 9500 Gilman Dr, La Jolla, CA 92093*

Darshan Sarojini[‡]
*Virginia Tech, 1600 Innovation Dr, Blacksburg, VA 24060*

Hyunjune Gill[§], Seongkyu Lee[¶]
*University of California Davis, 1 Shields Avenue, Davis, CA 95616*

Andrew Tagg, Ryan Anderson, Eric Green[‖], Cibin Joseph[**], Andrew Ning[††]
*Brigham Young University, Provo, UT 84602*

Zeyu Cheng[‡‡], Zhi Cao[§§], Chunting Mi[¶¶]
*San Diego State University, 5500 Campanile Dr, San Diego, 92182*

Alexandre T. R. Guibert[***], Ashley Cronk[†††], H. Alicia Kim[‡‡‡],
*University of California San Diego, 9500 Gilman Dr, La Jolla, CA 92093*

Y. Shirley Meng[§§§]
*The University of Chicago, Chicago, IL 60607*

Christopher Silva[¶¶¶]
*NASA Ames Research Center, Moffett Field, CA 94035*

John T. Hwang [17]
*University of California San Diego, 9500 Gilman Dr, La Jolla, CA 92093*

**Large-scale gradient-based Multidisciplinary Design Optimization (MDO) can aid in the exploration of high-dimensional design spaces for novel air vehicle concepts, thereby leading to more efficient and economic designs. This paper builds on past works where we demonstrated large-scale physics-based MDO capabilities and applied these to NASA's lift-plus-cruise electric**

[*]Ph.D. Students, Department of Mechanical and Aerospace Engineering, AIAA student members
[†]William Prager Professor, Department of Structural Engineering
[‡]Assistant Professor, Aerospace and Ocean Engineering Department, AIAA member
[§]Ph.D. Candidate, Department of Mechanical and Aerospace Engineering, AIAA student member
[¶]Professor, Department of Mechanical and Aerospace Engineering, AIAA associate fellow
[‖]Ph.D. Students, Mechanical Engineering, AIAA student members
[**]Postdoctoral Scholar, Mechanical Engineering, AIAA member
[††]Associate Professor, Mechanical Engineering, AIAA associate fellow
[‡‡]Ph.D. Student, Department of Electrical & Computer Engineering
[§§]Postdoctoral Researcher, Department of Electrical & Computer Engineering
[¶¶]Distinguished Professor and Chair, Department of Electrical & Computer Engineering
[***]Ph.D. Student, Structural Engineering Department, AIAA student member
[†††]Ph.D. Student, Materials Science & Engineering Program
[‡‡‡]Jacobs Scholar Chair Professor, Structural Engineering Department, AIAA associate fellow
[§§§]Professor of Molecular Engineering, Pritzker School of Molecular Engineering
[¶¶¶]Research Aerospace Engineer, Member AIAA
[17]Assistant Professor, Department of Mechanical and Aerospace Engineering, AIAA senior member

**air taxi concept. We extend this comprehensive mid-fidelity system-level optimization problem with high(er)-fidelity subsystem-level optimizations of various aircraft systems and mission phases, with the aim of further enhancing the accuracy and scope of the aforementioned system-level optimization problem: 1) Power minimization during the transition mission phase; 2) Electrical powertrain topology optimization; 3) Cell chemistry modeling and thermo-mechanical battery pack topology optimization; 4) Shell-based coupled aero-elastic wing structure optimization. An Analytical Target Cascading-like distributed MDO architecture allows us to couple the system- and subsystem-level optimizations in order to arrive at a consistent and feasible design. We find that the system-level design is most heavily impacted by the reduced battery pack-level energy densities that stem from power peaks in the mission profile. These power peaks seem to result from the inefficient lift rotor blade designs that are needed to satisfy noise constraints. We draw conclusions based on trends in our results and give recommendations for future MDO studies of electrical air taxi vehicle concepts.**

# I. Introduction

As the need for more efficient and environmentally-friendly air transport becomes more prevalent, aircraft designers have started considering more diverse vehicle concepts and propulsion systems. Among these are various (partially) electrified propulsion layouts and vehicle concepts that fall between fixed- and rotary-wing aircraft. Traditionally the initial, conceptual phases of aircraft design have been heavily based on empirical relations. Examples of reference works include those by Roskam [1], Raymer [2] and Torenbeek [3]. A limitation of such conceptual design approaches is that they rely heavily on data of similar aircraft being available. This restricts their usefulness to tried-and-tested vehicle concepts, thereby making design space exploration difficult.

In this work we consider the design of electrical Vertical Take-Off and Landing (eVTOL) vehicles for Urban Air Mobility (UAM) applications. There has been great interest in the design of such vehicles in recent years. Due to the absence of historical data for eVTOL vehicles a wide variety of vehicle concepts have been proposed and are being developed concurrently. This is evidenced by the eVTOL database of the Vertical Flight Society, which recently exceeded 1,000 [4] included vehicle concepts that have been proposed over the last 8 years. It remains an open question what vehicle concept and propulsion layout works best for eVTOL UAM. Large-scale Multidisciplinary Design Optimization (MDO) can help reduce the design space by using physics-based models to ascertain the performance of proposed vehicle concepts.

A significant number of works have focused on MDO and initial sizing for a diverse range of eVTOL vehicle architectures, in order to find answers for open questions on the optimality of such vehicles. We give a short list of examples of such works here. Various studies focus on low-fidelity physics-based and empirical models to compare initial sizing results of multiple eVTOL vehicle architectures [5–8]. Other works pick one or two specific architectures and focus on doing MDO of one or more subsystems in order to identify trends. Examples include comparisons of electrical and hybrid propulsion systems [9], aero-acoustics studies [10, 11] and acoustics & electrical propulsion design [12].

In previous studies we solved gradient-based large-scale MDO problems of the NASA lift-plus-cruise concept vehicle [13]. We initially considered over 100 design variables and 16 constraints in an optimization problem that utilized various low-fidelity physics-based models as well as regression-based structural weight estimation and a steady-state mission analysis with limited scope [14]. This optimization problem took only 30 minutes to solve with monolithic gradient-based optimization methods. Later we expanded on that by including physics-based structural beam and rotor-aerodynamics models, low-fidelity quasi-steady transition maneuvers and off-design operating conditions. This resulted in an optimization problem with over 300 design variables and over 200 constraints [15] that was solved in 17 hours.

This work expands upon the scope of our previous studies by extending the system-level optimization problem that was introduced in [15] with higher-fidelity subsystem-level optimizations. We use coupled Vortex Lattice Method-Blade Element Momentum theory (VLM-BEM) models to compute minimal-power trajectories of the transition phase between hover and climb; a component-level model to do powertrain topology optimization; a battery chemistry model and coupled thermo-mechanical model to minimize battery pack mass; and a Vortex Lattice Method (VLM) model coupled to a Reissner-Mindlin shell model to minimize wing structural mass. Optimal design data from these subsystem-level optimization problems is fed back to the system-level optimizer, which is then restarted. We use an Analytical Target

Cascading-like [16, 17] distributed MDO architecture to obtain consistency between the system- and subsystem-level optimizations, by adding a penalty term that penalizes inconsistency to the objective function of the system-level optimization. The penalty term weights are increased with each outer loop iteration in order to gradually tighten system consistency constraints.

The rest of this paper is structured as follows. We first give a brief overview in Sec. II of the system-level optimization problem that was initially presented by Ruh et al. in [15]. This is followed in Sec. III by the various subsystem-level optimization problems: Trajectory, powertrain, battery and aero-structural. References to related works are provided where necessary. Section IV covers the coupling approach between the system- and subsystem-level optimizations, as well as the methods used to estimate gross vehicle mass for the sub-optimizations, after which Sec. V covers the generated results. We focus on presenting trends between the various obtained optimal designs. Lastly, Sec. VI draws conclusions based on the results. We also give recommendations for future MDO studies of similar eVTOL air taxi concepts.

## II. System-Level Optimization

The system-level optimization problem solved in this paper involves a large number of disciplines and design conditions. Ruh et al. [15] specify in detail the optimization problem upon which the current system-level optimization is based, including design variables and constraints. We summarize the design conditions and models used in Tab. 1. We model all disciplines using low-to-mid fidelity physics-based models except for the motor and battery discipline, for which we use a Constant Power Density (CPD) model and an Energy Based Sizing (EBS) approach respectively. The rotor aerodynamics are described using Blade-Element Momentum (BEM) theory, whereas the fixed-wing aerodynamics are modeled with a VLM model. Euler-Bernoulli beam theory is used to model the wing structure as a box beam under applied aerodynamic loads. Sarojini et al. [18] verified the accuracy of the implementations of the aforementioned models, and compared their predictions to higher-fidelity models.

Our off-design conditions include two steady structural sizing conditions (+3g/-1g) and four One-Engine-Inoperative (OEI) conditions. For on-design conditions we consider hover, a quasi-steady transition, climb, cruise, and descent. We split up the transition segment of 80 seconds into 16-second segments and compute the time-averaged accelerations for each segment with the trajectory data that is computed by the high-fidelity trajectory optimization. We then constrain the quasi-steady transition points to match those of the time-averaged accelerations of each segment.

Other model inputs are tuned with the results of the high-fidelity subsystem optimizations that are covered in Sec. III. These include the battery energy density, powertrain efficiency for each mission segment and powertrain system mass. The wing thickness variables overlap with those of the high-fidelity aero-structural optimization, section IV.A covers how we enforce consistency between these two sets of design variables. Since the box beam wing approach used in this system-level optimization is limited in its accuracy, we correct its stress predictions and mass evaluations with the corresponding results of the aero-structural optimization. Corrective multiplicative factors for both are obtained by evaluating the stress and mass of the box beam for the optimal wing designs of the aero-structural optimization.

**Table 1 Summary of design conditions and physics-based models used in system-level optimization**

| **Condition** \ **Discipline** | *Rotor Aerodynamics* | *Wing Aerodynamics* | *Wing Structure* | *Aeroacoustics* | *Motor* | *Battery* |
|---|---|---|---|---|---|---|
| *+3g sizing* | BEM | VLM | EB beam | – | – | |
| *-1g sizing* | BEM | VLM | EB beam | – | – | |
| *OEI (x4)* | BEM | – | – | – | CPD | |
| *Hover* | BEM | – | – | Tonal: Lowson<br>Broadband: GL | CPD | EBS |
| *Quasi-steady transition (x5)* | Peters–He | VLM | – | Tonal: Lowson<br>Broadband: BPM | CPD | EBS |
| *Climb, cruise, descent* | BEM | VLM | – | – | CPD | EBS |

Since we use slightly different acoustics models than in our earlier work [15] we give a brief overview of them here. There are two approaches to determine tonal noise: frequency-domain and time-domain methods. The acoustic module in this optimization software utilizes Lowson-Ollerhead model for a frequency-domain method [19], which has been shown its effectiveness in rapidly predicting unsteady loading noise with fair accuracy in the previous studies [15, 18]. For the time-domain method, the software utilizes Farassat's Formulation 1A [20], which is an integral solution of Ffowcs Williams-Hawkings [21]. Its applications in various rotor configurations, combined with high-fidelity Computational Fluid Dynamics simulations, have shown superior accuracy in tonal noise predictions [22–25]. Since Formulation 1A requires time history of input parameters from an aerodynamic solver; however, it requires significantly larger amount of computing time per optimization cycle. Thus, the time-domain method is not used in this paper.

Three different broadband noise prediction models are available in the optimization software: Gill-Lee (GL) spectrum model [26], Brooks-Pope-Marcolini (BPM) model [27], and Amiet's trailing-edge noise theory [28]. It is known that a dominant rotor broadband noise source at high frequencies is turbulent boundary-layer trailing-edge noise [29]. The GL spectrum model is a data-driven empirical broadband noise model which was developed by applying an evolutionary machine learning algorithm, called gene expression programming. This model has shown its robustness across different rotor types, such as helicopter and small drone rotors, and demonstrated significantly improved broadband noise prediction accuracy compared to the existing models like Pegg [30] and Schlegel-King-Mull models [31]. However, the current version of the GL spectrum model is limited to hovering rotors. To overcome this limitation, the BPM model is utilized in axial and edgewise forward flight conditions. BPM model is an empirical model based on a series of experiments using the NACA 0012 airfoil. With a proper Doppler-effect correction, the model is extended to a rotor application to predict rotor broadband noise at axial and edgewise forward flight conditions. For a more accurate prediction of broadband noise, Amiet's trailing-edge noise theory [28] can be utilized, which is the method that has proven its effectiveness through numerous validations [32] and rotorcraft applications [33–36]. This method requires determination of wall pressure spectrum [37], which involves additional calculations and increases computational cost. In this paper, the GL spectrum model and BPM model are mainly used during the optimization.

The system-level optimization problem has been implemented in the toolbox Comprehensive Analysis and Design Environment for Engineering systems (CADDEE). CADDEE is a software framework designed to easily construct multidisciplinary models of aircraft and similar engineering systems in order to enable large-scale MDAO. This is made possible by several features:

1) *Design parameterization*: CADDEE uses a geometry-centric approach with a high-fidelity representation of the Outer Mold Line (OML). Basis splines are used due to their analytic form and their ability to smoothly represent complex geometries with a few number of control points. During optimization, CADDEE effectively propagates changes in the central geometry to physics-based solvers through the use Free-Form Deformation (FFD) and projections. A projection is the solution to an optimization problem to find the parametric coordinates corresponding to the minimum distance between points and the OML. Throughout optimization, the parametric coordinates do not change and therefore CADDEE can easily re-evaluate geometric quantities such as meshes or distances as the optimizer manipulates the FFD blocks. This is done through a simple matrix vector product of the basis matrix that is evaluated at the parametric coordinates and a vector of control points, which are manipulated by FFD.
2) *Modular data transfer*: CADDEE makes use of a Solver-Independent Field Representation (SIFR) to transfer data between solver disciplines. This approach is particularly important to efficiently solve coupling between disciplines such as aerodynamics and structural dynamics. At the core of this approach stands a central high-fidelity representation of the solver states that is defined over the boundary of components across which the states need to be transferred. An example is the skin of a wing and the load bearing internal structure such as the wing box. The SIFR representation is independent of the fidelity of the solver that is used to compute the states, which allows for solvers of different fidelity to be easily interchanged. Lastly, a critical feature of the SIFR approach is that it allows for force consistency and conservation of aeroelastic work.
3) *Comprehensive analysis*: CADDEE is able to model the entire aircraft across disciplines and multiple mission segments. Generally there are three types of mission segments that can be modeled, trim-state, transient and off-design. Trim-state segments are steady, on-design conditions such as hover, climb, and cruise and are typically easier to model as they are steady and do not size the aircraft. Transient conditions are generally unsteady (or quasi-steady) in nature and require time integration schemes. Examples are transition maneuvers or gust response dynamics, which are still on-design conditions. Such cases may contribute to the aircraft

sizing and may require more sophisticated physics-based simulations such as free-wake aerodynamic models and/or nonlinear dynamic structural models. Off-design conditions such as wing flutter, pull-up and push-down maneuvers, and OEI scenarios are the last type of mission segment that can be modeled with CADDEE. These kind of scenarios are unintended modes of operation and play a large role in sizing the aircraft structure.

4) *Automated adjoint-based sensitivity analysis*: CADDEE is implemented in a newly developed domain-embedded language called the Computational System Design Language (CSDL) [38], which is intended for building large models of engineering and solving MDAO problems using gradient-based techniques. CSDL operates at a high level of abstraction, allowing the engineer to use simple Python syntax to define mathematical operations, for which the computation of derivatives is fully automated. By implementing CADDEE using CSDL, we can systematically search a potentially high-dimensional design space, using gradient-based optimization to find the optimal (aircraft) design.

# III. High-Fidelity Subsystem Optimizations

We use various high(er)-fidelity subsystem models to augment the scope of the system-level optimization problem. These models are used to run subsystem-specific sub-optimizations. We utilize four such sub-optimization problems that cover the design and optimization of the following mission phases and subsystems:

1) Mission transition phase trajectory;
2) Electric powertrain;
3) Battery pack;
4) Wing structure.

We cover these sub-optimizations here in the order specified above.

## A. Transition Phase Trajectory

Fixed wing electric Vertical Takeoff and Landing (eVTOL) aircraft must pass through a difficult transition from hover to forward flight. This transition is marked by complex aerodynamics that are difficult to incorporate into the conceptual design stage. This is in part due to the change in rotor performance at different incidence angles [39], and in part due to unsteady wake interactions between different components of the aircraft [40]. Quasi-steady models such as BEM have been used to power gradient-based design optimization of blade design by assuming a prescribed transition trajectory [41]. The trajectory itself has been optimized using simplified aerodynamics models [42]. Trim states along the transition have been identified using simplified aerodynamics that ignore wake interactions [43], or by fitting a surrogate to higher-fidelity CFD models [44] or to wind tunnel data [45]; however, these approaches do not fully capture the unsteady wake behavior. To our knowledge, optimization of the transition trajectory using CFD-grade unsteady aerodynamic models has yet to be performed. One reason for this is the high computational cost of obtaining gradients of high-fidelity CFD.

Controlling an eVTOL aircraft through transition is likewise difficult, as the aircraft dynamics change significantly over the transition envelop. Model predictive control methods have been shown to be successful if the changing aircraft dynamics can be captured [46]. Controls strategies typically leverage gain scheduling, changing the tuning parameters and sometimes the fundamental control strategy throughout the trajectory [47], though unified, fully nonlinear controls strategies have been achieved, allowing the same control strategy to be used throughout the trajectory so long as intermediate waypoints can be identified. [48]. Optimal control strategies such as incremental nonlinear dynamic inversion has been demonstrated to reduce the control effort required to follow a path, and is popular for eVTOL aircraft [49]. It should be noted that path-following on its own does not result in an optimal trajectory, but rather the optimal control inputs to follow a commanded trajectory.

In this work, we present a novel approach to trajectory optimization using expensive high-fidelity modeling approaches. The approaches consists of an inner control loop, which leverages optimal control strategies to minimize control effort, and an outer optimization loop that optimizes the commanded trajectory. Using this approach, we are able to optimize the eVTOL transition trajectory while accounting for fully unsteady wake effects.

### *1. Aerodynamic model*

The aerodynamic model used in this work is a conventional Vortex Lattice Method (VLM) coupled with Blade Element Momentum Theory (BEMT). The VLM is used to calculate aerodynamic forces and moments on the lifting surfaces of the aircraft, and BEMT is used to calculate thrust and torque on each rotor. These two methods are coupled through the wake induced by the rotors, which is resolved with BEMT. These induced velocities are applied to the lifting surfaces and included in the VLM solution. This method allows for mid-fidelity calculations of rotor-surface interactions as the aircraft moves through its trajectory.

*2. Trajectory optimization*

The trajectory optimization objective consists of finding a set of optimal control inputs $u^*$ that are required to obtain a set of optimal states $x^*$. Together, these control inputs and states result in the trajectory that minimizes power input to the system. In this method, two optimization loops are implemented. The problem statement follows the form of a discrete LQR controller as shown in Eq. (1)

$$\begin{aligned} \text{minimize} \quad & [x^T u^T] P \begin{bmatrix} x \\ u \end{bmatrix} \\ \text{with respect to} \quad & x, u \\ \text{subject to} \quad & \dot{x} = Ax + Bu \\ & x_f = x_{\text{cruise}} \end{aligned} \tag{1}$$

Where $P$ is a matrix that defines a quadratic penalty on power input, $A$ and $B$ are the result of the linearized system equations of motion, and $x_f$ is the final state of the trajectory, which must equal the desired cruise state $x_{\text{cruise}}$. Note that $x$ and $u$ are vectors defined over the time horizon. Therefore the objective function projected over the entire horizon becomes

$$P = [x_0^T x_1^T \ldots u_0^T u_1^T \ldots] \begin{bmatrix} P_0 & & \\ & \ddots & \\ & & P_n \end{bmatrix} \begin{bmatrix} x_0 \\ x_1 \\ \vdots \\ u_0 \\ u_1 \\ \vdots \end{bmatrix}$$

Likewise, the linearized equations of motion over the time horizon become

$$\begin{bmatrix} x_1 \\ x_2 \\ \vdots \end{bmatrix} = \begin{bmatrix} 0 & & & \\ A_1 & \ddots & & \\ & \ddots & 0 & \\ & & A_n & 0 \end{bmatrix} \begin{bmatrix} x_1 \\ x_2 \\ \vdots \end{bmatrix} + \begin{bmatrix} B_0 & & \\ & \ddots & \\ & & B_n \end{bmatrix} \begin{bmatrix} u_0 \\ u_1 \\ \vdots \end{bmatrix} + \begin{bmatrix} A_0 \\ 0 \\ \vdots \end{bmatrix} x_0$$

The $P$, $A$ and $B$ matrices are calculated at every time step, creating a linear time variant (LTV) system that is linearized about the vehicle's most recent trajectory. These matrices are then updated at each iteration of the optimization until convergence is achieved. From the system-level optimization we use as inputs the vehicle mass and inertia tensor components in order to describe the vehicle's dynamic response to the input loads. These loads are defined through the locations and geometries of the various rotors, wing and tail surfaces that are taken from the system-level optimization as well. We emphasize that we constrain the transition trajectories in this work to be fully horizontal.

## B. Powertrain Topology

Various electric propulsion architectures have been proposed for electric aircraft, including all-electric, hybrid-electric, and turbo-electric systems [50]. The powertrain model used in this work aims to minimize the gross mass of the entire aircraft and facilitate the integration of motor and battery models. The following sections describe various aspects of the computational model of the powertrain system. Unless otherwise indicated the equations presented here are taken from [51]. Figure 1 presents a high-level diagram of the powertrain system analyzed in this study, which is based on the powertrain architecture of NASA's X-57 Maxwell [52]. The term "powertrain" in this work is used to denote the power electronics that connect the battery to the various electrical motors, its function is to convert the Direct Current (DC) power coming from the battery into consistent Alternating Current (AC) power.

We consider the powertrain as three distinct parts, each with distinct but interconnected roles. The DC bus acts as the primary power source for the inverters, typically consisting of capacitors that stabilize and filter the DC voltage in order to minimize voltage ripples and transient disturbances from upstream sources (in this case the battery pack). Inverters convert the DC power from the DC bus into AC power to drive the motors. They use semiconductors such as MOSFETs or IGBTs to perform high-speed switching in order to achieve efficient DC-to-AC conversion. Filters are positioned at the output of the inverters to smooth the AC waveforms and reduce harmonics generated by the high-frequency switching. This protects the motors by mitigating Electromagnetic Interference (EMI) and minimizing bearing currents. In this way the powertrain components ensure a reliable and efficient power supply for the electric motors, maintaining power quality and protecting system components.

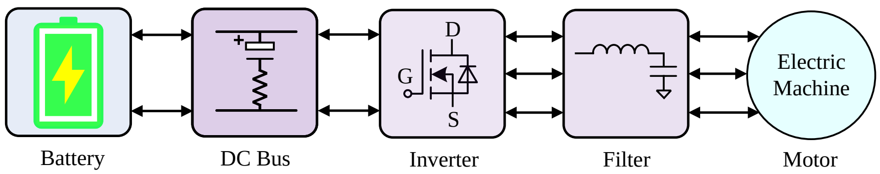


**Fig. 1 Powertrain system layout, connecting the battery pack to the motors**

The DC bus, inverter and filter are made up of various smaller components. Figure 2 gives an overview of the components that are taken into account in our powertrain model. In the next sections we cover the models that dictate the behavior of these components. Some related works that deal with eVTOL aircraft powertrain modeling are [53, 54].

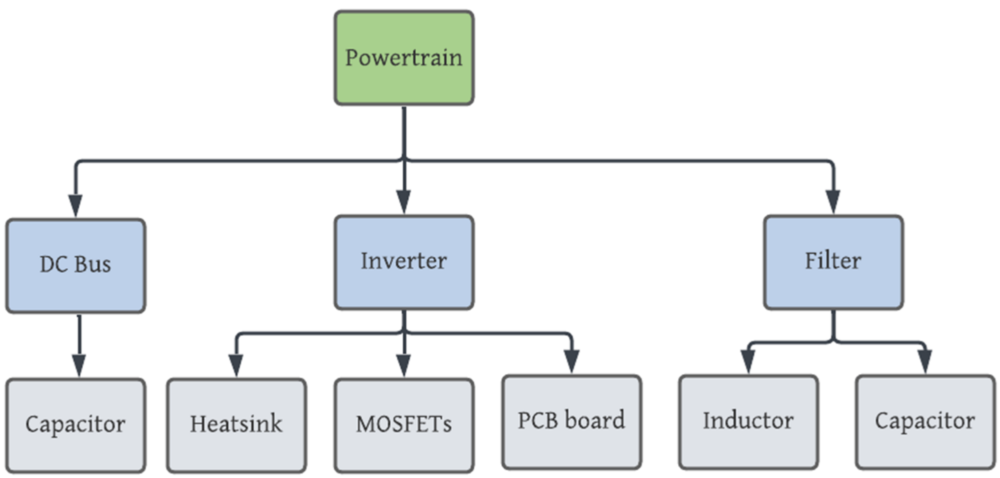


**Fig. 2 Components per part of the powertrain system**

*1. Inverter Topology Selection*

Choosing an appropriate inverter topology and powertrain architecture based on the configuration, size, and power demands of eVTOL aircraft is crucial. Figure 3 illustrates the main schematic of the topologies examined in this study. This paper evaluates three inverter topologies: the two-level (2L) inverter, the three-level Active Neutral Point Clamping (3L-ANPC) inverter, and the three-level T-type (3L-T) inverter, as shown in Figure 3a, Figure 3b, and Figure 3c, respectively. To evaluate the performance of the inverter, the mathematical model for calculating the RMS current of each device is presented. For example, in a 2L inverter, based on the area equivalence principle, the RMS current of S1 in the positive half of the cycle can be calculated using

$$I_{\mathrm{S1,rms,p}} = \sqrt{\frac{1}{T_s}\int_0^{d_{\mathrm{ave}}T_s} I_{\mathrm{rms}}^2 dt} = I_{\mathrm{rms}}\sqrt{d_{\mathrm{ave}}}, \tag{2}$$

and the RMS current of S1 in the negative half of the cycle can be calculated using

$$I_{\mathrm{S1,rms,n}} = \sqrt{\frac{1}{T_s}\int_{d_{\mathrm{ave}}T_s}^{T_s} I_{\mathrm{rms}}^2 dt} = I_{\mathrm{rms}}\sqrt{1-d_{\mathrm{ave}}}. \tag{3}$$

In both these equations the average duty ratio of switch $d_{\mathrm{ave}}$ can be computed with

$$d_{\mathrm{ave}} = \frac{1}{\pi}\int_0^{\pi} D_{\mathrm{max}} sin(\omega t) d(\omega t) = \frac{2D_{\mathrm{max}}}{\pi}, \tag{4}$$

where $T_s$ is the switching period, $I_{\mathrm{rms}}$ is the RMS value of current, and $D_{\mathrm{max}}$ is the maximum duty ratio. For other inverter topologies, the calculation method follows Eq. 2 through Eq. 4, with adjustments to the limits of integration based on the Pulse-Width Modulated (PWM) signal waveform.

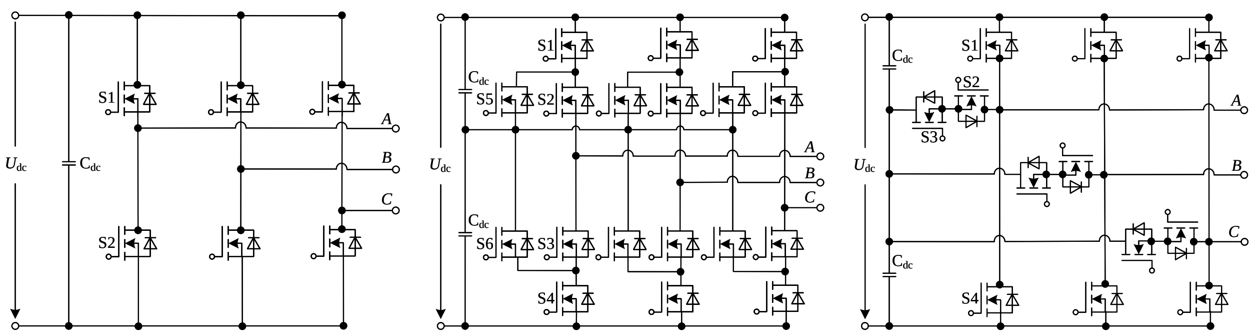


**(a) Two-level inverter** **(b) Three-level ANPC inverter** **(c) Three-level T-type inverter**

**Fig. 3 Considered inverter topologies**

*2. Semiconductor Model*

Depending on the aircraft specifications and inverter topologies, different technologies and voltage rating semiconductors can be selected. In this work only Wide Band-Gap (WBG) devices are studied, due to their better performance than devices of other technology types. The conduction losses $P_{\mathrm{cond}}$ and switching losses $P_{\mathrm{sw}}$ are calculated using

$$\begin{aligned} P_{\mathrm{cond}} &= I_{\mathrm{rms}}^2 R_{\mathrm{ds,on}}, \\ P_{\mathrm{sw}} &= \frac{1}{2} C_{\mathrm{oss}} V_{\mathrm{ds}}^2 + \frac{1}{6} V_{\mathrm{ds}} I_{\mathrm{rms}} f_{\mathrm{sw}} (t_{\mathrm{on}} + t_{\mathrm{off}}). \end{aligned} \tag{5}$$

Here $R_{\mathrm{ds,on}}$ is the turn-on resistance of the semiconductor, $C_{\mathrm{oss}}$ is the output capacitance, and $t_{\mathrm{on}}$ and $t_{\mathrm{off}}$ are the rise time and fall time, respectively. These four parameters are extracted from the semiconductor datasheet. $V_{\mathrm{ds}}$ is the drain-source voltage, $f_{\mathrm{sw}}$ is the switching frequency, and $I_{\mathrm{rms}}$ is the Root-Mean Square (RMS) current through the device. These three parameters depend on the working conditions and the selection of inverter topologies. All devices are assumed to operate at a constant temperature.

*3. Inductor Model*

The design of an inductor can be divided into two parts: magnetic component design and winding design. The magnetic component design is based on inverter topologies, losses, and the reluctance model. To calculate the inductor losses, the inductor geometry is divided into separate regions to construct a reluctance network, as illustrated in Figure. 4a, where an EE-shaped magnetic core is shown. The resulting Magnetic Equivalent Circuit (MEC) model of a three-phase inductor is shown in Figure. 4b. A nonlinear iteration method is employed in the MEC model to account for the magnetic saturation effects; this iteration method is depicted in Figure. 5. The improved generalized Steinmetz equation (iGSE) [55] is used to calculate the core losses $P_{\text{core}}$ as

$$P_{\text{core}} = \frac{1}{T}\int_0^T k_i \left|\frac{dB}{dt}\right|^2 (\Delta B)^{\beta-\alpha} dt, \tag{6}$$

where $\alpha$, $\beta$, and $k_i$ are Steinmetz parameters. $\Delta B$ represents the peak-to-peak magnetic flux density across each region.

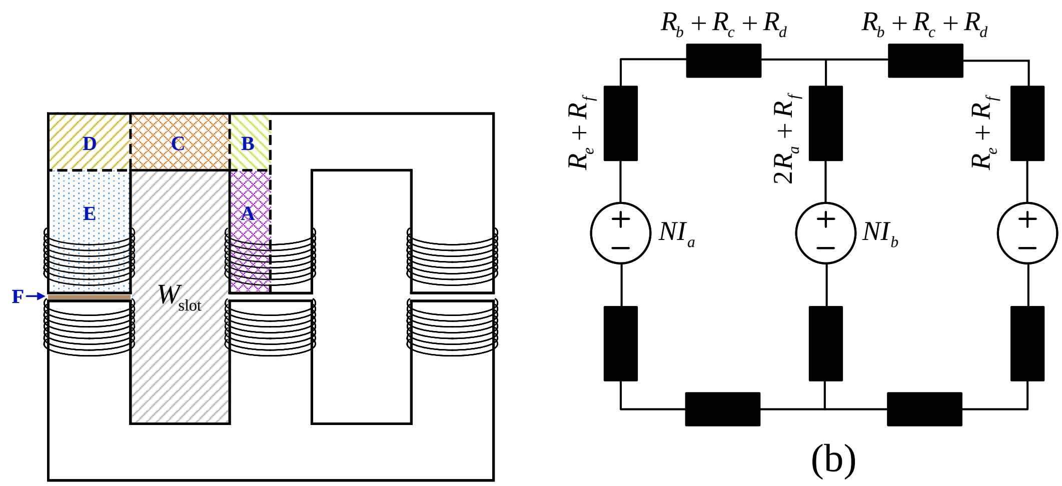


**(a) EE core geometry for reluctance calculation**

**(b) Magnetic Equivalent Circuit**

**Fig. 4 Reluctance network modeling and resulting MEC**

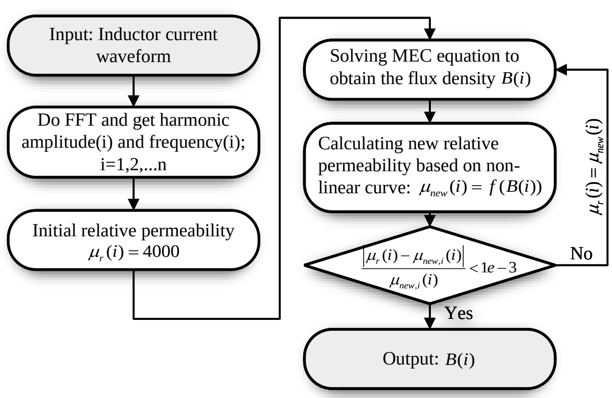


**Fig. 5 Magnetic Equivalent Circuit nonlinear iteration approach**

The design of the winding is based on the current density, core shape, and saturation flux density. A constant current density is assumed to determine the winding diameters. The number of turns $N$ is calculated with

$$N = \frac{I_{\max} L}{B_{\max} A_c}. \tag{7}$$

where $I_{\max}$ is the maximum current, $L$ is the inductance, $B_{\max}$ is the saturation flux density, and $A_c$ is the cross-sectional area. The winding constraint equation, given by

$$2NA_{\text{w}} \leq K_{\text{s}} W_{\text{slot}}, \tag{8}$$

states that the total copper area must be less than the slot area $W_{\text{slot}}$. The constant slotting factor $K_s$ is assumed to be 0.7.

Litz wire is the only type considered in this study, due to its lower winding losses compared to other types of winding. The analytical model for winding losses, which takes into account the skin effect, is constructed following [56], as

$$P_{\text{winding}} = nR_{\text{dc}}F_R(f)\left(\frac{I_L}{n}\right)^2. \tag{9}$$

Here $n$ is the number of strands, $R_{\text{dc}}$ is the winding DC resistance; $F_R(f)$ is a factor that describes the increases of DC resistance due to the skin effect.

*4. Remaining Component Models*

1) *Cooling system*: Various cooling systems can be considered in the powertrain model. The optimizer evaluates different cooling methods during the optimization process to identify the method that results in the minimum heat sink mass while meeting temperature constraints. We consider here air cooling through forced convection over an extruded-fin heat sink [57] and two-phase liquid cooling [58]. The thermal resistance of the heat sink is calculated using the thermal equivalent circuit method. The maximum allowable heat sink thermal resistance is determined through

$$R_{\text{th,hs}} = \frac{T_{\text{hs}} - T_{\text{amb}}}{P_{\text{loss}}}, \tag{10}$$

where the maximum allowed heat sink plate temperature $T_{\text{hs}}$ is restricted to 105 ℃ , and the maximum ambient temperature $T_{\text{amb}}$ is 35 ℃. The mass of the heat sink is calculated based on its geometry. Figure 6 shows the relevant geometrical parameters for both considered heat sink types; these are included as variables in the powertrain optimization.

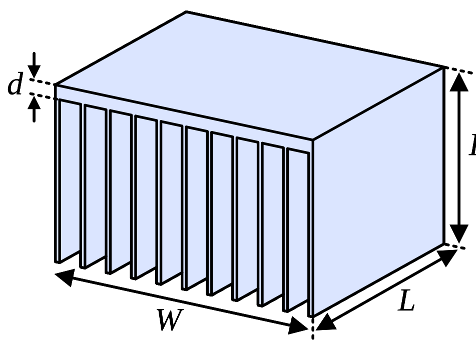


**(a) Extruded-fin air cooling heat sink**

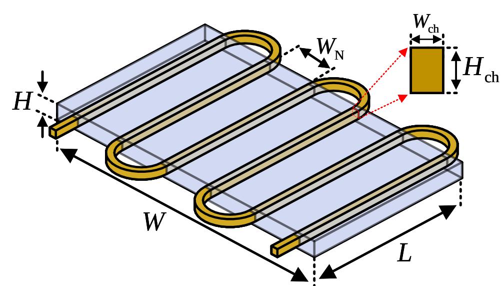


**(b) Two-phase liquid cooling plate**

**Fig. 6 Considered heat sink geometries**

2) *Capacitors*: In the powertrain model, only ceramic and film capacitors are considered due to their high power density and reliability. We can estimate the mass of the capacitors with

$$m_{\text{cap}} = kV_r^{\alpha}C^{\beta}V_{\text{c}}, \tag{11}$$

where $k$, $\alpha$, $\beta$ are parameters related to different types of capacitors and can be found in [59]. The capacitance $C$, voltage rating $V_r$, and volume of the capacitor $V_c$ can be extracted from the capacitor datasheets.

3) *Auxiliary electronics*: Auxiliary electronics include the gate driver, control board, and other auxiliary electronic components in the inverter. In this powertrain model, auxiliary power losses and auxiliary mass are assumed to be constant.

*5. Optimization Routine*

The objective of the powertrain optimization is to minimize the combination of powertrain mass $m_{pt}$ and (approximate) battery mass $\hat{m}_{batt}$. All other vehicle mass contributions are assumed to be constant under changes in the powertrain. The powertrain mass is calculated directly, while the effects of the powertrain on battery mass are approximated with

$$\hat{m}_{\text{batt}} = \sum_i \frac{E_i}{\rho_{\text{batt}}} \frac{1}{\eta_{\text{pt,i}}}, \tag{12}$$

where $i$ is the mission segment index, $E_i$ is the energy usage per mission segment, $\rho_{\text{batt}}$ is the pack-level battery energy density and $\eta_{\text{pt,i}}$ is the powertrain efficiency per mission segment. The powertrain optimization problem is then given by

$$\begin{aligned} &\text{minimize} && m_{\text{pt}} + \hat{m}_{\text{batt}} \\ &\text{with respect to} && \mathbf{x} \\ &\text{subject to} && p_i(\mathbf{x}) \leq 0, i = 1, ..., n_p \\ & && m_i(\mathbf{x}) = 0, i = 1, ..., n_m \end{aligned} \tag{13}$$

where $m_{\text{pt}} + \hat{m}_{\text{batt}}$ is the objective function, subject to $n_p$ inequality constraints $p_i(\mathbf{x})$ and $n_m$ equality constraints $m_i(\mathbf{x})$. The design variables $\boldsymbol{x}$ and other constant inputs are summarized in Table 2. The motor's electrical frequency and the feasible operating range of WBG devices determines the lower and upper bounds of the switching frequency. Powertrain efficiency fluctuates with varying power demands in each mission segment. Therefore, optimizing the rated output power of the inverter is essential to achieve the highest possible powertrain efficiency across the entire mission profile. The range of the inverter's rated output power, $P_o$, is determined by the aircraft configurations and the potential power range required for the given mission profile. Based on empirical data, the current density in each conductor is assumed to be between 5 $A/mm^2$ and 6 $A/mm^2$. Therefore, the boundary range of winding diameters can be determined by the current density range. The range of inductor and heat sink geometry variables is based on the dimensions of products currently available on the market. The bound range of the inverter topology is defined by the number of inverters included in this optimization problem. Whereas most of the design variables are continuous, some (such as the inverter topology) are discrete or not differentiable (such as the choice of heat sink type). As such we resort to using a gradient-free optimization approach. We leverage a combination of Simulated Annealing and a Genetic Algorithm to obtain optimal powertrain designs that lead to the lowest gross vehicle mass.

**Table 2 Design variables and constant inputs**

| Design variable | Variable range |
|---|---|
| Inverter topology $T_{\text{i}}$ | $1, 2, 3$ |
| Switching frequency $f_{\text{sw}}$ | $[20\ kHz, 200\ kHz]$ |
| Ripple attenuation factor RAF | $[0.001, 0.6]$ |
| Invertor rated output power $P_{\text{o}}$ | $[15\ kW, 60\ kW]$ |
| Inductor winding diameter on inductor side $d_{\text{i}}$ | $[2\ mm, 10\ mm]$ |
| Inductor winding diameter on motor side $d_{\text{g}}$ | $[2\ mm, 10\ mm]$ |
| Heat sink height $H$ | $[40\ mm, 80\ mm]$ |
| Heat sink width $W$ | $[100\ mm, 150\ mm]$ |
| Heat sink length $L$ | $[151\ mm, 201\ mm]$ |
| Number of air cooling heat sink fins $n$ | $[10, 50]$ |
| Liquid cooling channel height $H_{\text{ch}}$ | $[0.5\ mm, 3\ mm]$ |
| Liquid cooling channel width $W_{\text{ch}}$ | $[0.5\ mm, 3\ mm]$ |

## C. Battery Pack

The modeling and design of battery packs play a crucial role in advancing the maturity, assessing the safety, and increasing the performance of eVTOL vehicles. Therefore, it is essential to capture the battery cell-level and pack-level responses to given flight profiles and power requirements. We take these into account through a two-step modeling and optimization approach: First we model the response of the battery cells to a given mission power profile. The cell heat generation is then provided as input to a battery pack topology optimization model. As shown in Figure 7, the battery pack is split over the four booms that connect the lift rotors to the aircraft wings. Also shown in the detail view is the initial shape of a unit cell of the load-carrying and heat-dissipating battery packs, prior to any topology optimization.

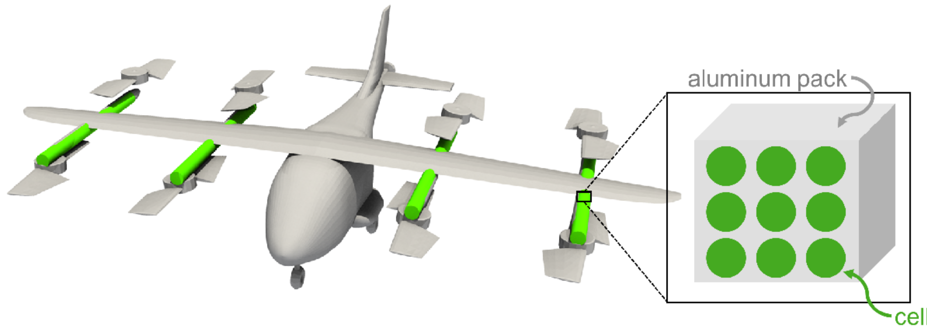


**Fig. 7 Layout of battery cells in rotor booms with detail view of cells inside rotor booms prior to topology optimization**

Various physics-based electrochemical models with different levels of fidelity can be used to model the response of battery cells to a given power profile. In order of increasing fidelity: the Single Particle Model (SPM) [60], the Single Particle Model with electrolyte (SPMe) [61], and the Doyle-Fuller-Newman model (DFN) [62]. These models are derived from charge and mass conservation in the cell and are implemented within the open-source Python-based battery modeling and simulation library PyBaMM [63]. In this work we use the DFN model to compute whether a given battery pack layout can deliver the power profile required for the design mission. If this is found not to be the case, additional rows of cells are added iteratively in parallel until the sized-up battery is able to complete the given power profile. Since the rows of cells are added in parallel this does not affect nominal system voltage. This procedure results in an appropriately-sized battery pack configuration to feasibly complete the design mission.

We use a battery cell model that is based on the LG M50 cell model in PyBaMM of Chen et al. [64]. We use a nominal voltage of 3.6 $V$ and capacity of 4.85 $Ah$. With a cell mass of 0.07 $kg$ this results in a cell-level energy density of 250 $Wh/kg$. In order to draw a better comparison with the works of Sarojini et al. [14] and Ruh et al. [15] on which much of this work is based, we assume an initial pack-level energy density of 400 $Wh/kg$. Silva et al. [13] assume the same. They estimate that 30% of the battery mass is used by battery management systems and packaging. We resolve the battery packaging explicitly in this work, as described below. We assume that half of the aforementioned battery mass increase (15%) is used by packaging. To then match the 400 $Wh/kg$ pack-level energy density used in prior work [14, 15], we assume a cell-level energy density of 460 $Wh/kg$. This cell-level energy density includes the mass contribution of battery management systems. In order to be consistent with the aforementioned works of Sarojini et al. [14] and Ruh et al. [15] we use an allowable depth of discharge of 80%, between 90% and 10% state of charge. The peak cell heat generation is passed to the battery pack topology optimization algorithm.

The battery pack response is predicted with a steady-state thermo-mechanical finite element model [65] implemented with the open-source finite element package FEniCS [66]. The model assumes a weak coupling between the heat transfer and the linear elasticity problems. This is reasonable under the small deformation assumption. Therefore, the coupled problem is solved sequentially. First, the steady heat conduction problem is solved for the temperature distribution. Then, a linear elasticity problem is solved considering the thermal strain due to the temperature increase and the mechanical loading due to the aircraft rotors, taken to be equal to $1/7^{\text{th}}$ of the vehicle weight (to account for OEI conditions).

The battery pack design is optimized using the level-set topology optimization method implemented with the open-source software ParaLeSTO [67]. The topology optimization is carried out for a battery unit cell that contains nine battery cells, arranged in a $3 \times 3$ grid in a block of $70 \times 90 \times 90$ $mm^3$. with mesh cells of 1 $mm$ in each direction, this leads to $2,840,000$ degrees of freedom. The objective of the optimization problem is to minimize the mass of the battery pack given temperature and packaging volume constraints, the latter in order to bound the packaging mass from above. We add 0.1 times the structural compliance to the objective function as a penalization term in order to obtain a fully-connected packaging topology. Consequently, the optimization problem reads

$$\begin{aligned} \min_{\Omega} \quad & m_{\text{batt}} + 0.1 C_s \\ \text{subject to} \quad & T_p \leq \bar{T} \\ & \mathbf{R} = \mathbf{0} \end{aligned}$$

where $m_{\text{batt}}$ is the mass of the battery pack, $C_s$ is the structural compliance, $T_p$ is the maximum temperature with a $p$-norm aggregation function, and $\mathbf{R}$ denotes the residual vector of the electrochemical and thermo-mechanical models. The temperature upper bound $\bar{T}$ is equal to 30° Celsius (303.15 Kelvin).

The two-step battery pack optimization procedure is connected to the system-level optimization by updating the pack-level battery energy density. These updates reflect changes in cell heat generation over the course of the mission power profile, and the number of cells that are needed to generate the required power draws.

### D. Wing Structural Design

We carry out a coupled aero-elastic optimization to design a lightweight wing structure. For the aerodynamic model, we use the same VLM model that is used in the system-level optimizer and couple it to a linear Reissner-Mindlin (RM) shell model. Sarojini et al. [18] covered the code verification of these and many other computational models used within this work. Moreover, this RM shell model has been coupled to the same VLM model in various past works [68, 69]. A machine-learning based airfoil model is used to find the pressure distribution on the wing skin given the VLM lift and drag values [70]. The RM shell model is implemented in FEniCSx [71]; the automatic differentiation capabilities of FEniCSx are integrated into CADDEE through the Finite Elements for Multidisciplinary Optimization (FEMO) library [72]. This allows us to perform gradient-based high-fidelity aeroelastic optimization of the wing structure with the SLSQP optimization algorithm. Moreover, FEMO's inclusion in CADDEE allows us to leverage SIFR for modular aeroelastic coupling [69, 73].

In line with the objective of the system-level optimization, the objective of the aero-structural sub-optimization problem is to minimize the wing mass. The system-level optimization handles wing shape optimization, whereas the high-fidelity aero-structural optimization focuses on thickness optimization on a shell mesh of the shape-optimized wing. Shell models are very well-suited for this since their discretization does not depend on local thicknesses. Given a set of material parameters we modify the thicknesses of the wing skin (16), spars (16) and ribs (9), for a total of 41 design parameters. Figure 8 shows the distribution of wing skin sections; each upper and lower bay between neighboring ribs has a constant wing skin thickness. The same holds for the spars, with each of the two spars being divided into constant-thickness sections between neighboring ribs.

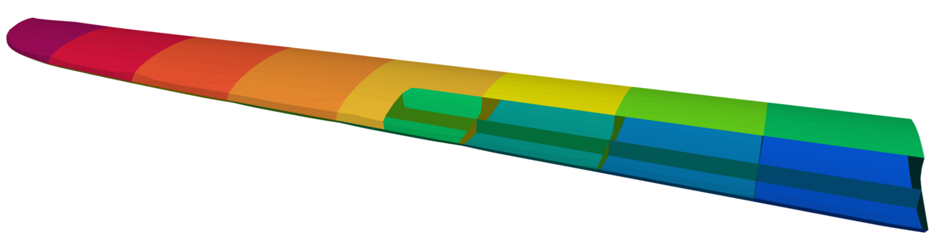

**Fig. 8 Cutaway view of a single wing, each color denotes a wing skin section with constant thickness**

To manage the computational cost of the aero-structural optimization we do two preliminary numerical tests. First we compare optimized wing designs that are obtained with two- and one-way aero-elastic coupling. In the former the RM shell and VLM models are solved alternatingly, both feeding updated displacement and force information to one another until the coupled system reaches a converged state. In the latter approach we compute the aerodynamic forces of the undeformed wing and impose these onto the RM shell, without using the deformed wing shape to re-compute the aerodynamic forces. Table 3 shows the tip displacement, peak stress, trimmed angle of attack and wing structural mass of the optimized designs that were obtained with both coupling approaches. As can be seen the difference between them is small. We thus opt for using a one-way-coupled aero-elasticity approach in the rest of this work, for the sake of computational efficiency.

**Table 3 Optimal wing structural design data obtained with one- and two-way aero-elastic coupling**

| Coupling | Tip displacement [m] | Peak stress [MPa] | Angle of Attack [deg] | Wing mass [kg] |
|---|---|---|---|---|
| One-way | 0.1336 | 33.72 | 1.234 | 131.09 |
| Two-way | 0.1385 | 33.30 | 1.344 | 131.63 |

Next we test three meshes of varying sizes in order to quantify how fine the shell mesh should be. Figure 9 shows the three considered meshes: A baseline mesh with $2,486$ cells and two steps meshes that are twice as fine in each direction as the previous mesh, resulting in meshes that have four and sixteen times as many cells respectively. Table 4 shows the wing tip displacements and peak stresses that are obtained for a specific load case with these three meshes. We see that, as the mesh is refined, the tip displacement decreases while the peak stress increases; the latter is due to a stress concentration near the wing root that becomes more pronounced as the local cell size is decreased. The peak stresses are significantly lower than the material yield stress, and the tip displacement variations are less than 5%. Hence we proceed with using the baseline mesh for our optimizations.

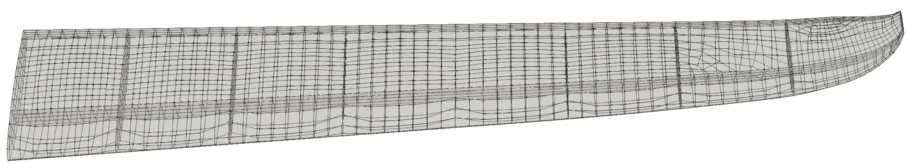

**(a) 2,486 cells**

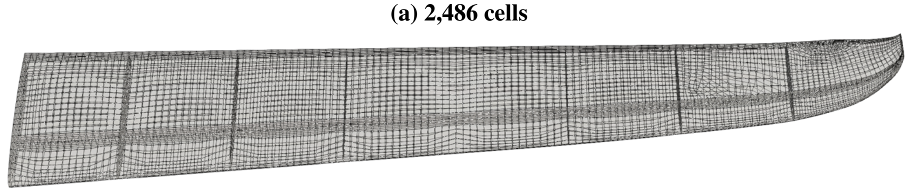

**(b) 9,872 cells**

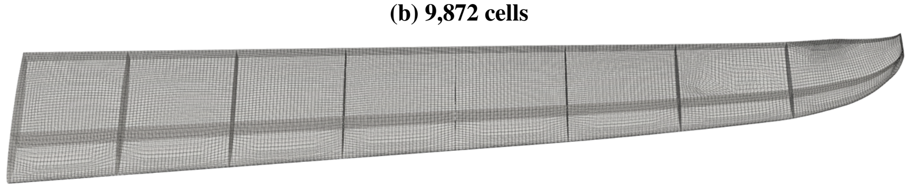

**(c) 39,488 cells**

**Fig. 9 Coarse, medium and fine wing shell meshes**

**Table 4 Structural wing response of a single load case with meshes of three different sizes**

| Number of mesh cells | Tip displacement [m] | Peak stress [MPa] |
|---|---|---|
| 2,486 | 0.04800 | 29.98 |
| 9,872 | 0.04778 | 32.63 |
| 39,488 | 0.04603 | 37.67 |

In the optimizations we consider static $+3g$ and $-1g$ load cases. The coupled aero-elastic system is trimmed at these load cases via a bracketed Angle of Attack search. We include the inertial loads of the rotor booms at their corresponding locations on the wing. Buckling constraints are imposed on a per-surface basis. The buckling stress is computed analytically with Roark's formula for curved panels under uniform compression [74, Tab.15.2, 13.a, p.734],

$$\sigma' = \frac{1}{6}\frac{E}{1-\nu^2}\left[\sqrt{12\left(1-\nu^2\right)\left(\frac{t}{r}\right)^2 + \left(\frac{\pi t}{b}\right)^4} + \left(\frac{\pi t}{b}\right)^2\right]. \tag{14}$$

Here $E$ and $\nu$ are the Young's modulus and Poisson ratio. Geometric parameters consist of panel thickness $t$, the width $b$ of the curved panel and the radius of curvature $r$ corresponding to the panel curvature. Maximum stress constraints of 350 $MPa$ were found to more lax than the buckling constraints, and were thus removed from the optimization problem. Post-optimality checks showed that all optimal designs shown in this work satisfy the excluded maximum stress constraints.

## IV. Distributed Multidisciplinary Design Optimization

We couple the sub-optimizations of section III to the system-level optimization covered in section II. We do this with a distributed MDO architecture. Using these sub-optimizations in a distributed MDO architecture (as opposed to monolithic) has two main advantages. It allows us to take into account vastly different optimization problems without greatly increasing the cost of solving the system-level optimization problem, and makes it possible to use different optimization algorithms that are each tailored to specific problem types. For an example of the former: The battery pack optimization involves solving a topology optimization problem with millions of design variables, whereas the other optimization problems have several hundreds of design variables at most. An example of the latter is the powertrain optimization, which involves discrete design variables; as such we need to use a gradient-free optimization algorithm to solve it, as opposed to the more efficient gradient-based algorithms used elsewhere. In section IV.A we first cover the way in which the various optimization problems are coupled to one another. Following that, section IV.B discusses how the gross vehicle mass and subsystem masses are estimated with updated data from each optimization.

### A. Optimization Coupling

Section III covers what information is transferred between the system-level optimization and the subsystem-level optimizations. We use the hierarchical Jacobi-style coupling approach shown in Fig. 10. Each sub-optimization is run at the same time, after which their relevant data is fed back to the system-level optimizer, which then recomputes the optimal vehicle design. To obtain a feasible optimal design that is consistent between all optimizations we use Analytical Target Cascading (ATC). ATC was first introduced by Kim et al. [16] as a way of propagating design requirements and targets through a hierarchical system. Tosserams et al. [17] extended this to non-hierarchical systems, having MDO in mind. ATC enforces consistency between optimizations with shared variables and constraints by introducing penalty terms to the objective functions of the system- and subsystem-level optimizations. These penalty terms scale with the differences between variables that are shared between multiple optimizations. By increasing the weights of the penalty terms after each outer loop iteration we ensure that the distributed MDO problem converges to a consistent and feasible optimal design. Martins and Lambe [75] give more details on ATC and cite various example applications in aerospace and beyond. An eVTOL application of ATC can be found in [76].

The objective functions of each subsystem optimization align with the system-level optimization, and the design variables and constraints of the system optimization and trajectory, powertrain & battery pack optimizations are disjoint. Only the aero-structural wing optimization shares design variables and constraints with the system-level optimization problem. In our implementation of ATC we defer to the higher-fidelity aero-structural wing sub-optimization when evaluating stress constraints that are shared with the system-level optimization. We do this by scaling the shared stress constraints in the system-level optimization, such that the optimal design of the aero-structural sub-optimization is considered feasible. Both optimization models use the wing box thicknesses as design variables. We enforce consistency between both optimizations by penalizing in the system-level optimization model any deviations from the optimal solution of the aero-structural optimization of the previous outer loop. Let $\boldsymbol{t}_{\text{struct}}^{(k-1)}$ denote the optimized wing box thickness vector of the aero-structural optimization model in outer loop iteration $k-1$, whereas $\boldsymbol{t}_{\text{system}}^{(k)}$ denotes the current wing box thickness vector in the system-level optimization of outer loop iteration $k$. We define the inconsistency vector as

$$\boldsymbol{c}^k\left(\boldsymbol{t}_{\text{system}}^{(k)}\right) = \boldsymbol{t}_{\text{system}}^{(k)} - \boldsymbol{t}_{\text{struct}}^{(k-1)}, \tag{15}$$



Author version · cite the published paper: doi.org/10.2514/6.2025-0362

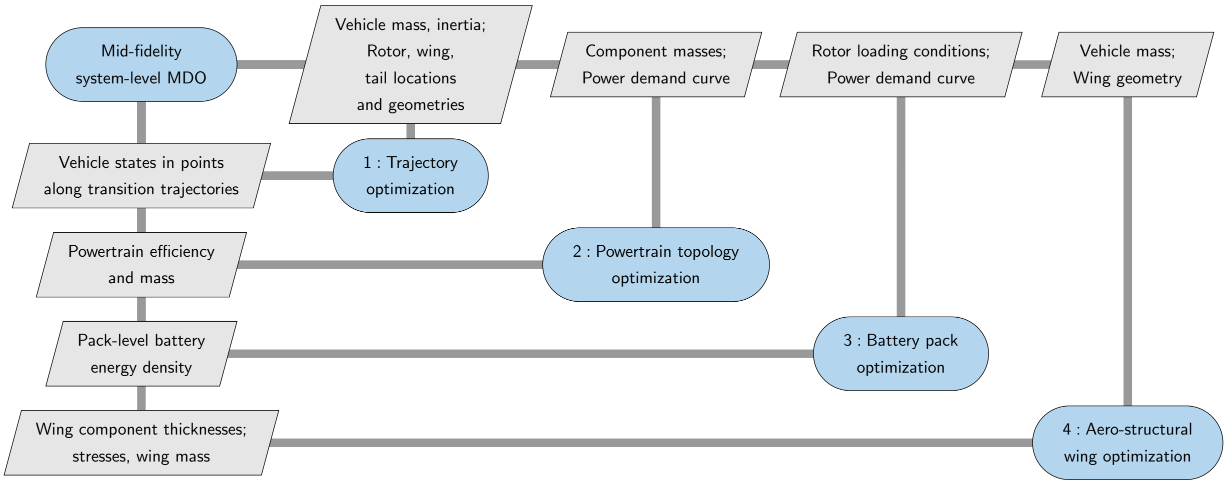


**Fig. 10 Jacobi-style coupling between system-level optimization and subsystem optimizations**

and define the corresponding penalty term $\Pi^{(k)}\left(\boldsymbol{t}^{(k)}_{\text{system}}\right)$ in the objective function of the system-level optimization as

$$\Pi^{(k)}\left(\boldsymbol{t}^{(k)}_{\text{system}}\right) = \rho^{(k)}\left[\left(\boldsymbol{v}^{(k)}\right)^T \boldsymbol{c}^{(k)} + ||\boldsymbol{w}^{(k)} \circ \boldsymbol{c}^{(k)}||_2^2\right]. \tag{16}$$

Here $\circ$ denotes element-wise multiplication of vectors. The penalty parameters $\rho^{(k)}$, $\boldsymbol{v}^{(k)}$ and $\boldsymbol{w}^{(k)}$ are defined as

$$\begin{aligned} \rho^{(k)} &= \frac{1}{\exp\left[\sqrt{\left(S^{(k)}_{\text{system}} - S^{(k-1)}_{\text{system}}\right)^2 + \left(AR^{(k)}_{\text{system}} - AR^{(k-1)}_{\text{system}}\right)^2}\right]}, \\ \boldsymbol{v}^{(k)} &= \boldsymbol{v}^{(k-1)} + 2\boldsymbol{w}^{(k-1)} \circ \boldsymbol{w}^{(k-1)} \circ \boldsymbol{c}^{(k-1)}, \\ \boldsymbol{w}^{(k)} &= \beta \boldsymbol{w}^{(k-1)}. \end{aligned} \tag{17}$$

Where $S_{\text{system}}$ and $AR_{\text{system}}$ are the wing area and aspect ratio. Note that $S^{(k)}_{\text{system}}$ and $AR^{(k)}_{\text{system}}$ vary during the system-level optimization of outer loop iteration $k$, whereas $S^{(k-1)}_{\text{system}}$ and $AR^{(k-1)}_{\text{system}}$ are constant. Including this scaling term lets us reduce the penalization $\Pi^{(k)}$ when the system-level optimizer changes wing design parameters that do affect the optimal wing box thicknesses, but that aren't shared with the aero-structural sub-optimization. We choose $\beta = 2.5$ as scaling parameter for $\boldsymbol{w}$ and initialize the penalization in the second outer loop iteration with $\boldsymbol{v}^{(2)} = \mathbf{0}$ and $\boldsymbol{w}^{(2)} = \mathbf{1000}$.

### B. Subsystem Optimization Vehicle Mass Estimation

Gross vehicle mass is affected by the various parameters that are fed back to the system-level optimization by the subsystem optimizations. The subsystem optimization models do not possess any inherent knowledge of the mass of the entire vehicle, since they only consider specific parts or aspects of the vehicle. We thus construct approximate gross vehicle mass models, in order to aid in judging convergence of the distributed MDO problem and the effects of the subsystem optimizations on the overall vehicle. We split up the gross vehicle mass into the following components:

- Powertrain electronics $m_{\text{pt}}$,
- Electrical motors $m_{\text{motor}}$,
- Battery pack $m_{\text{batt}}$,
- Wing structure $m_{\text{wing}}$,
- Non-wing structures $m_{\text{nws}}$,
- Other (payload, assorted aircraft systems) $m_{\text{o}}$.

Such that in outer loop iteration $k$,

$$m_{\text{vehicle}}^{(k)} = m_{\text{pt}}^{(k)} + m_{\text{motor}}^{(k)} + m_{\text{batt}}^{(k)} + m_{\text{wing}}^{(k)} + m_{\text{nws}}^{(k)} + m_o. \tag{18}$$

The system-level optimization is based on that of Ruh et al. in [15], and as such has the same breakdown of gross vehicle mass into constituent systems. We add to that a mass term that accounts for the mass of the powertrain electronics (i.e. $m_{\text{pt}}$). The non-wing structural mass $m_{\text{nws}}$ thus consists of the fuselage, rotor boom and empennage mass shown in [15]. "Other" mass $m_o$ consists of the mission payload and assorted non-structural aircraft systems and does not change from iteration to iteration. The non-wing structural mass fraction $m_{\text{nws}}/m_{\text{vehicle}}$, wing mass fraction $m_{\text{wing}}/m_{\text{vehicle}}$ and electrical motor mass fraction $m_{\text{motor}}/m_{\text{vehicle}}$ are kept constant for all subsystem optimizations per outer iteration loop. Note that below we don't cover the mission transition phase trajectory optimization, since that does not directly affect the gross vehicle mass in our models. In the next sections quantities without the word *new* in their subscript are those computed by the system-level optimization.

### 1. Powertrain Topology Optimization

In outer loop iteration $k$ a new value for the powertrain electronics mass $m_{\text{pt, new}}^{(k)}$ and powertrain efficiencies $\eta_{\text{pt},i}^{(k)}$ (indexed according to mission segment $i$) are computed by the powertrain topology optimization. With the updated efficiencies we recalculate the battery mass as

$$\hat{m}_{\text{batt}}^{(k)} = \sum_i \frac{E_i^{(k)}}{\rho_{\text{batt}}^{(k)}} \frac{\eta_{\text{pt},i}^{(k-1)}}{\eta_{\text{pt},i}^{(k)}}. \tag{19}$$

Here $E_i^{(k)}$ is the battery energy needed for mission segment $i$, and $\rho_{\text{batt}}^{(k)}$ is the current pack-level battery energy density. The updated battery mass $\hat{m}_{\text{batt}}^{(k)}$ is thus the result of the battery mass required to complete each mission segment, weighted by the ratio of the old and new powertrain efficiency for that same mission segment. A more efficient powertrain thus reduces the required battery mass. We point out that the old powertrain efficiencies $\eta_{\text{pt},i}^{(k-1)}$ are sourced from the system-level optimization and are identical to the output of the powertrain optimization in outer loop $k-1$. The updated vehicle mass $m_{\text{vehicle,pt}}^{(k)}$ after the powertrain topology optimization then becomes

$$m_{\text{vehicle,pt}}^{(k)} = \frac{m_{\text{pt, new}}^{(k)} + \hat{m}_{\text{batt}}^{(k)} + m_{\text{o}}}{1 - \frac{m_{\text{nws}}^{(k)}}{m_{\text{vehicle}}^{(k)}} - \frac{m_{\text{wing}}^{(k)}}{m_{\text{vehicle}}^{(k)}} - \frac{m_{\text{motor}}^{(k)}}{m_{\text{vehicle}}^{(k)}}}. \tag{20}$$

### 2. Battery Pack Optimization

The only mass component directly affected by the battery pack optimization is $m_{\text{batt}}$. Let $m_{\text{batt,new}}^{(k)}$ denote the newly computed battery pack mass. Then the updated vehicle mass $m_{\text{vehicle,batt}}^{(k)}$ is

$$m_{\text{vehicle,batt}}^{(k)} = \frac{m_{\text{pt}}^{(k)} + m_{\text{batt,new}}^{(k)} + m_{\text{o}}}{1 - \frac{m_{\text{nws}}^{(k)}}{m_{\text{vehicle}}^{(k)}} - \frac{m_{\text{wing}}^{(k)}}{m_{\text{vehicle}}^{(k)}} - \frac{m_{\text{motor}}^{(k)}}{m_{\text{vehicle}}^{(k)}}}. \tag{21}$$

We also point out that the pack-level battery energy density $\rho_{\text{batt,new}}^{(k)}$ is updated.

### 3. Aero-Structural Wing Optimization

Unlike the other sub-optimizations we don't use the wing mass ratio $\frac{m_{\text{wing}}}{m_{\text{vehicle}}}$, since we directly compute the wing structural mass $m_{\text{wing,new}}^{(k)}$ in the aero-structural wing optimization. The updated vehicle mass $m_{\text{vehicle,wing}}^{(k)}$ becomes

$$m_{\text{vehicle,wing}}^{(k)} = \frac{m_{\text{pt}}^{(k)} + m_{\text{batt}}^{(k)} + m_{\text{o}}}{1 - \frac{m_{\text{nws}}^{(k)}}{m_{\text{vehicle}}^{(k)}} - \frac{m_{\text{motor}}^{(k)}}{m_{\text{vehicle}}^{(k)}}}. \tag{22}$$

Note that we don't update the battery mass, since we're not modifying the mission profile energy usage.

*4. Combining Subsystem Optimization Data*

After running the subsystem optimizations we make an estimate of the gross vehicle mass breakdown with all updated information from the subsystem optimizations. The battery mass is estimated as

$$m^{(k)}_{\text{batt, combined}} = \sum_i \frac{E^{(k)}_i}{\rho^{(k)}_{\text{batt, new}}} \frac{\eta^{(k-1)}_{\text{pt},i}}{\eta^{(k)}_{\text{pt},i}}, \tag{23}$$

which then leads to the following gross vehicle mass estimate

$$m^{(k)}_{\text{combined,new}} = \frac{m^{(k)}_{\text{pt,new}} + m^{(k)}_{\text{batt,combined}} + m^{(k)}_{\text{wing,new}} + m_{\text{o}}}{1 - \frac{m^{(k)}_{\text{nws}}}{m^{(k)}_{\text{vehicle}}} - \frac{m^{(k)}_{\text{motor}}}{m^{(k)}_{\text{vehicle}}}}. \tag{24}$$

# V. Results

With multiple runs each of five optimization models we have an extensive amount of data. Our focus in this work is on how the returned outputs of the subsystem optimizations affect the system-level optimization results, and how this in turns affects the subsystem optimizations. As such we highlight here trends in the optimized designs between outer loop iterations. We first report on the wall time of each optimization in section V.A. Next, in section V.B, we look at the change in estimated gross vehicle mass after each optimization. The system-level optimization trends are covered in section V.C, followed by the subsystem optimizations in section V.D. Lastly we look at the design parameter consistency between the system-level and aero-structural optimizations in section V.E.

## A. Optimization Wall Times

Table 5 shows the approximate wall times of each optimization problem in the order in which they were run. Since the Jacobi-style coupling approach allows us to run all subsystem optimization simultaneously, the total wall time per iteration is the sum of the system-level optimization and the maximum of the subsystem optimizations. As can be seen the system-level optimization currently takes the most time, and needs more time to converge in later iterations, owing to the difficulty of finding feasible designs with lower battery energy densities, as is covered below. The trajectory, battery pack and aero-structural models all speed up as the iterations progress, due to their warm-start capabilities with gradient-based optimization techniques. The powertrain optimization does not benefit from this, and thus its gradient-free optimizer carries out the same number of design iterations during each optimization.

**Table 5 Approximate wall times of each optimization per iteration, and total turnaround time per Jacobi iteration**

| Optimization | System-level | Trajectory | Powertrain | Battery pack | Aero-structural | Iteration total |
|---|---|---|---|---|---|---|
| Baseline | - | 5 $hrs$ | 4 $hrs$ | - | - | 5 $hrs$ |
| Iteration 1 | 15 $hrs$ | 5 $hrs$ | 4 $hrs$ | 7 $hrs$ | 3.33 $hrs$ | 22 $hrs$ |
| Iteration 2 | 17 $hrs$ | 4 $hrs$ | 4 $hrs$ | 4 $hrs$ | 0.1 $hrs$ | 21 $hrs$ |
| Iteration 3 | 17 $hrs$ | 2 $hrs$ | 4 $hrs$ | 3 $hrs$ | 0.1 $hrs$ | 21 $hrs$ |

## B. Vehicle Mass Evolution

We compare the gross vehicle mass predictions resulting from the various optimizations. The system-level optimization directly computes the vehicle mass; section IV.B covers how we update the estimated vehicle mass following each subsystem optimization. Figure 11 shows the (estimated) system mass breakdowns corresponding to each optimization. The leftmost bar of each iteration is the system-level optimization, followed by the powertrain, battery pack, and aero-structural optimizations, with lastly a mass estimation that combines all updated subsystem-level information. Compared to the initial system-level optimization of iteration 1 (which we treat as baseline), the battery pack model leads to an increase in gross vehicle mass of roughly 100 $kg$. The high-fidelity aero-structural wing optimization reduces wing mass by 300 $kg$, with snowball effects leading to a weight decrease of 350 $kg$. Combining their data again leads to a decrease in estimated vehicle mass of 270 $kg$.

Feeding back the optimized subsystem data to the system-level optimization results in another mass increase, this time from $3,827\ kg$ in iteration 1 to $4,145\ kg$ in iteration 2. As is covered in the next section this updated design uses significantly more power and energy, which causes the vehicle mass in the subsequent battery pack optimization to increase significantly, thereby increasing the corresponding vehicle mass by 640 $kg$ with respect to the system-level optimization of iteration 2. Again the aero-structural optimization finds a lower-mass wing design, leading to a vehicle-level mass decrease of 90 $kg$. The combined mass estimate is again higher, this time exceeding the system-level optimization by 550 $kg$.

The combined mass estimate of iteration 2 is similar to the actual mass of the system-level optimization in iteration 3. Again in iteration 3 the vehicle mass in the battery pack optimization is significantly larger, due to an increase in battery pack mass of 430 $kg$ relative to the system-level optimization. This causes the related gross vehicle mass to increase by 640 $kg$. The aero-structural and powertrain mass estimations are both similar to the system-level vehicle mass, to within 20 $kg$. As a result of the battery pack mass increase, the combined vehicle mass estimate also exceeds the system-level vehicle mass, by 620 $kg$, slightly lower than the battery pack optimization mass.



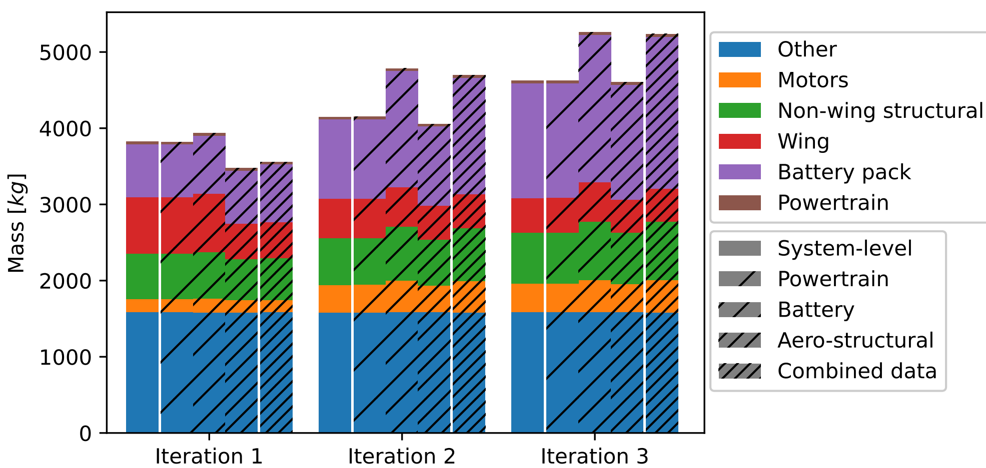


**Fig. 11 Estimated system mass breakdowns after each optimization**

### C. System-level Optimization Results

We highlight here some trends from the system-level optimization results. Figure 12 shows the power profiles corresponding to one mission leg of the optimal vehicle design of each iteration. The vertical dashed lines show where each mission segment ends. These segments are in order of hover, transition maneuver, climb, cruise and descent. We note that the power profile labeled "iteration 1" was obtained with the optimal trajectory labeled "baseline" in section V.D.1, the power profile label "iteration 2" was obtained with the optimal trajectory labeled "iteration 1" in section V.D.1, and similar for iteration 3. Even though gross vehicle mass between iterations 1 and 2 increases by only 12.5%, the power draw in iteration 2 while hovering is 46% larger. Similarly, the peak power draw during the transition maneuver increases by 104%. Climb power increases by 28%, while the cruise and descent power changes are only 13% and $-1$% respectively. We point out the large power increases specifically during mission segments that employ the lift rotors. These increases are significantly higher than the theoretical scaling of power as function of thrust to the power of $\frac{3}{2}$. This indicates that the optimized lift rotors in iteration 2 are significantly less efficient than those of iteration 1. The hover power growth between iterations 2 and 3 matches the theoretical scaling.

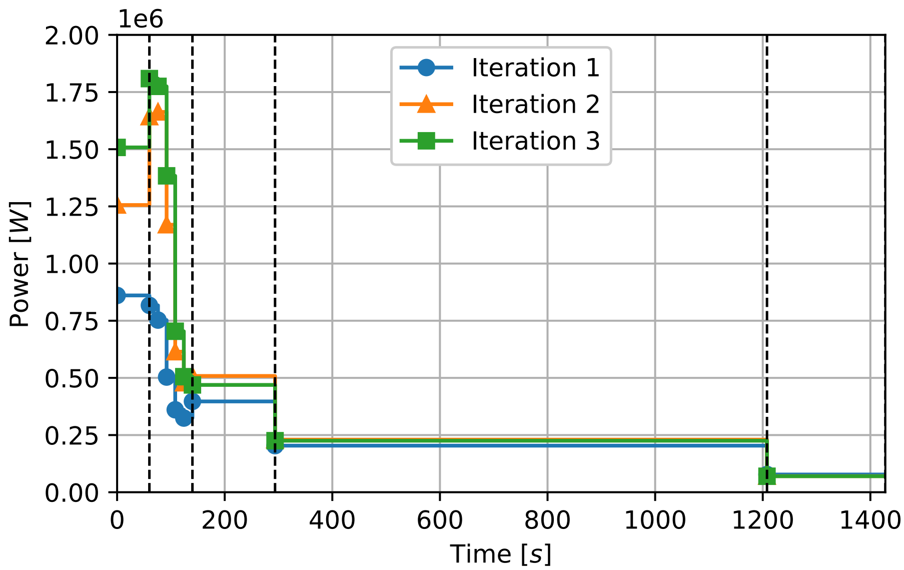


**Fig. 12 Mission power profiles of system-level optimization per outer loop iteration; shown in succession are hover, transition maneuver, climb, cruise and descent mission segments**

This large power increase between iterations 1 and 2 seems to be caused by the noise constraints: These are all active, and as a result seem to limit the efficiencies of the lift rotor blades above a certain disk loading threshold. It seems like the noise constraints limit how much lift force can be generated with the lift rotors at reasonable power levels: Increasing the required lift force once the noise constraints are active comes at the cost of needing significantly more power to drive the lift rotors. Heavier eVTOL vehicles designed to operate at acceptable noise levels for urban environments could potentially benefit from using higher numbers of lift rotors, or using more blades per rotor in order to spread the required loads over more rotors and rotor blades. We look at three mature eVTOL Urban Air Mobility concepts as points of comparison. The Maximum Take-Off Weights (MTOWs) of the vehicle designs presented in this work fall between $3,500 - 5,000\ kg$ and all use 8 lifting rotors. Joby's S4 vehicle [77] is estimated to have a MTOW of $2,400\ kg$ with 6 lifting rotors. Archer's Midnight aircraft [78] is estimated to be at a MTOW of $3,200\ kg$ with 12 lifting rotors. Wisk's Generation 6 pre-production prototype [79] is quoted as having a comparable payload weight as the S4 and Midnight, and uses 12 lifting rotors. These vehicles each have payload weights less than half of our designs, resulting in significantly lower MTOWs even with current battery technology. Consequently, the required lift per rotor is smaller than our current vehicle designs. This seems to suggest that in the presence of constant noise constraints a trend exists, where the number of lift rotors should increase with gross vehicle mass in order to avoid having to resort to inefficient rotors.

Figure 13 shows breakdowns of the mass of the system-level-optimized vehicle into the various considered systems. We regard the vehicle obtained in iteration 1, shown in figure 13a, as baseline for the system-level optimizations. As mentioned previously the mass component designated as "other" remains constant. The mass of the electric motors increases significantly from iteration 1 to iteration 2, owing to the related significant increase in maximum power. While the motor mass increases from iteration 2 to 3 as well, this increase is small compared to the gross vehicle mass increase. This again indicates that, starting from iteration 2, the (active) noise constraints force the optimizer to use relatively inefficient rotor blades. Battery pack mass increases from iteration to iteration, both due to higher energy capacity requirements and decreases in pack-level energy density; section V.D.3 covers these trends in more detail. Wing mass decreases gradually from iteration to iteration, both in absolute terms and relative to gross vehicle mass. This happens due to the more accurate wing stress evaluations of the high-fidelity aero-structural optimization, which are passed to the system-level optimization and effectively enlarge the feasible space for the wing thicknesses. Lastly, the non-wing structural mass shows slight increases in absolute terms, but this is smaller than the mass increase of other vehicle

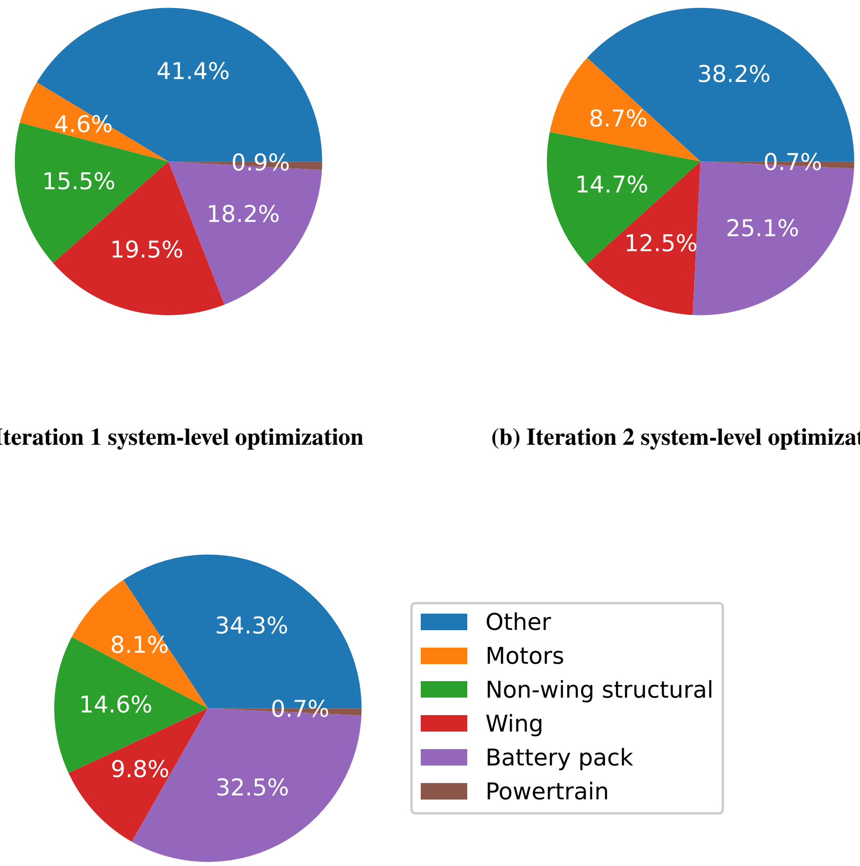


**(a) Iteration 1 system-level optimization**

**(b) Iteration 2 system-level optimization**

**(c) Iteration 3 system-level optimization**

**Fig. 13 System mass breakdowns of system-level-optimized Lift+Cruise vehicle per outer loop iteration**



components, thereby reducing its share of the gross vehicle mass.

## D. Sub-Optimization Results

### *1. Transition Trajectory*

Figure 14 shows the velocity, acceleration and pitch angle along the optimized trajectories of the transition maneuver between the hover and climb mission segments. Shown are the data of the baseline trajectory that was generated before running the system-level optimization of iteration 1, as well as the trajectories computed during iterations 1 and 2 (which were subsequently used during iterations 2 and 3 of the system-level optimization) and iteration 3. The velocity of the baseline trajectory shows a more rapid increase during the initial stage of the trajectory and associated higher acceleration during this period, inherited in part from its starting nonzero acceleration. The subsequent three trajectories show more gradual velocity increases, owing to their relatively constant accelerations.

Negative pitch corresponds to a nose-down maneuver. Looking at the pitch angle variations we see that some of the trajectories (iterations 1 and 2) pitch forward faster than others, in order to induce more thrust and acceleration from the forward rotation of the lift rotors. After the initial push towards a nose-down pitch angle the pitch angle is gradually

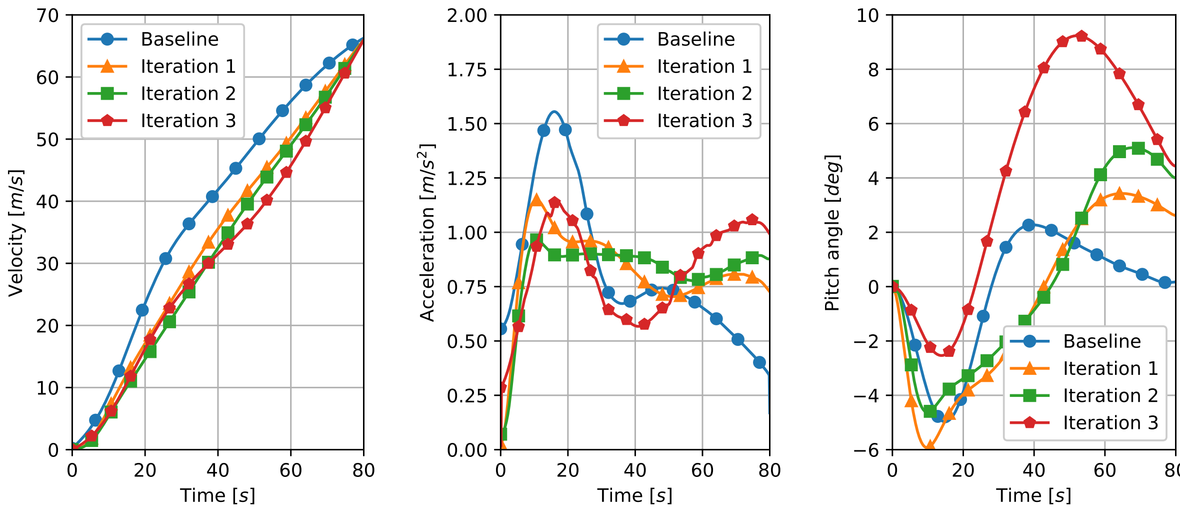


**(a) Velocity** **(b) Acceleration** **(c) Pitch angle**

**Fig. 14 Velocity, acceleration and pitch angle along optimized transition maneuver trajectories**

turned positive in order to make use of the potential for wing-based lift force that appears with the growing velocity. While the baseline trajectory ends at a pitch angle close to zero, the subsequent optimized trajectories all attain final pitch angles between 2 and 5 degrees.

### *2. Powertrain Topology*

The efficiencies per mission segment of the optimized powertrain systems are shown in figure 15a. We generate baseline efficiencies by using a standard lift + cruise vehicle, which are used for the initial system-level optimization. The efficiency of the optimized powertrain in iteration 1 is superior to the baseline for each mission segment. In subsequent iterations we can see the efficiency loss due to high power demands, this is especially reflected in the efficiency of the hover and transition segments. Cruise efficiency is being prioritized by the optimizer, due to cruise being the biggest contributor to energy usage. For each iteration the optimal inverter topology is the three-level ANPC inverter. Figure 15b shows the associated powertrain system mass. As can be seen, iteration 1 improves upon the baseline's system mass, whereas subsequent iterations lead to small powertrain mass increases.

### *3. Battery Pack Design*

Figure 16 shows the battery state of charge and cell voltage over the course of both legs of the mission profile. As is visible in figure 16a, the initial state of charge is 90% while the final state of charge exceeds 20% and increases from iteration to iteration. This is due to the battery pack needing to be enlarged because of high power draws: With any smaller battery pack the cells would not be able to complete the power profile without failing. This can also be seen when looking at the cell voltages in figure 16b: Around 1500 seconds into the mission (during the second hover and transition segments) the cell voltages drop close to the cutoff of 2.5 $V$ due to the high power draws. We thus have usable battery energy left at the end of the design mission. Testing with our battery chemistry model shows that it would be possible to extend the cruise segment of the design mission by 30% at the cost of only 1.3% extra battery pack mass, and by 50% at a cost of 2.6% extra battery pack mass. Only enough additional cells need to be added to ensure that the second hover and transition segments do not result in cell voltages below 2.5 $V$. From this we conclude that high cell C-rates are mainly important for eVTOL vehicles with shorter missions and smaller cruise ranges. After all, longer cruise segments require more energy and hence battery cells, which allows the peak power draws of hover and transition segments to be spread over more cells, thereby lowering the resulting C-rates.

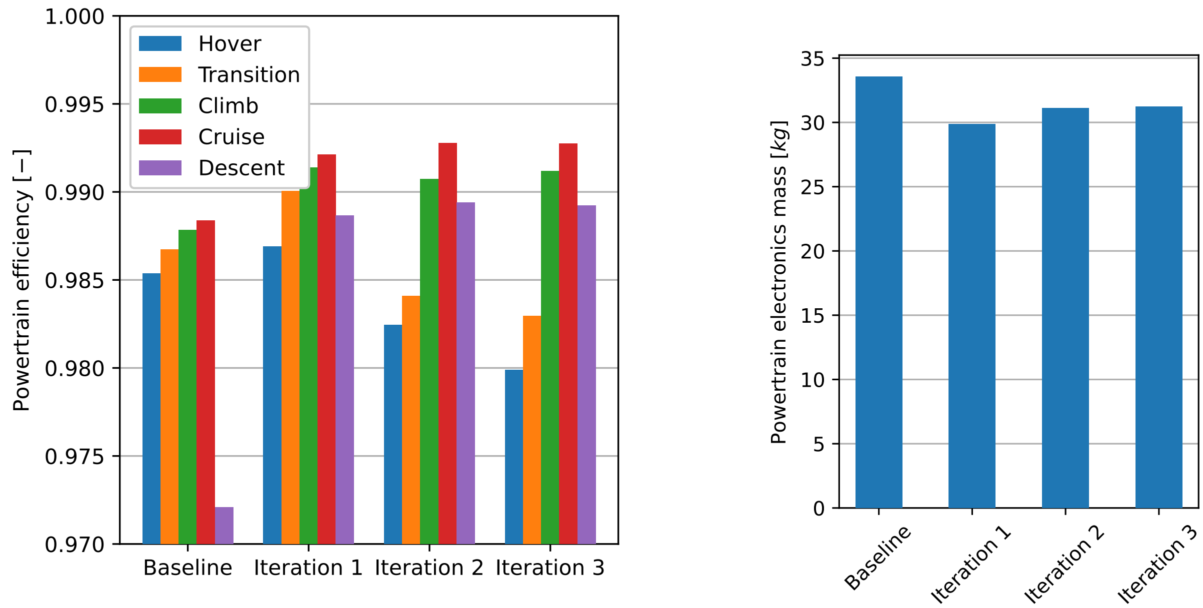


(a) Powertrain efficiency per mission segment

(b) Powertrain system mass per iteration

**Fig. 15 Optimization powertrain efficiency per mission segment and powertrain system mass for each run of the powertrain optimization model**

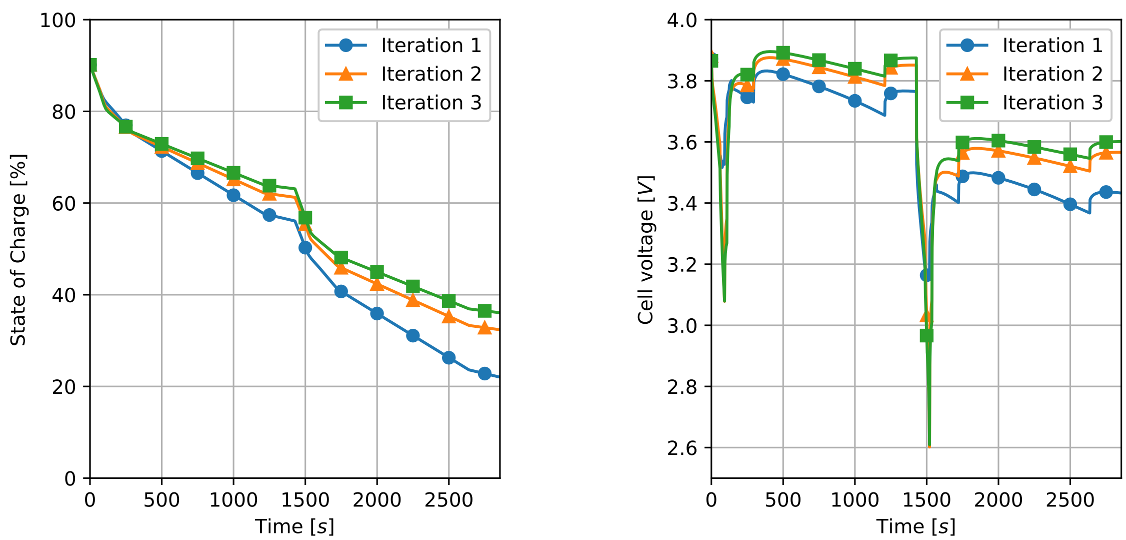


(a) State of Charge

(b) Cell voltage

**Fig. 16 State of Charge and cell voltage during both mission legs**

Figures 17, 18 and 19 show the topology-optimized battery pack designs of iterations 1 and 2 respectively. Around the $3 \times 3$ battery cell grid we can see the structural elements that transfer the thermal loads (from the cells to the surrounding structure) and mechanical loads (from the structure to the cells). The packaging mass overhead factor (i.e., the mass of the cells plus packaging divided by the cell mass) during iteration 1 (as shown in figure 17 is only 1.12, close to the assumption of 15% of Silva et al. in [13]. During iterations 2 and 3 the peak cell heat generation is more than double that of iteration 1. Moreover, the mechanical loading is larger, owing to the increased vehicle mass. Because of this the packaging factors rise to 1.5 and 1.72 during iterations 2 and 3 respectively. These packaging factors are high because of several reasons:

- First, the temperature limit of 30° Celsius is strict and could realistically be raised without reaching the thermal limits of lithium-ion battery cells.
- Second, we use a steady-state thermo-mechanical model and use the maximum instantaneous cell heat generation to size the battery packaging. Repeating the same optimization with a transient model could lower the cell temperatures due to thermal mass effects and reduce the compliance. The work of Yan et al. [80] is one example of a comparison between steady-state and transient thermo-mechanical topology optimization.
- Third, the mechanical loading scales with vehicle mass. The heavier vehicles of iterations 2 and 3 induce more deformation of the battery pack, necessitating more packaging mass to increase pack stiffness.

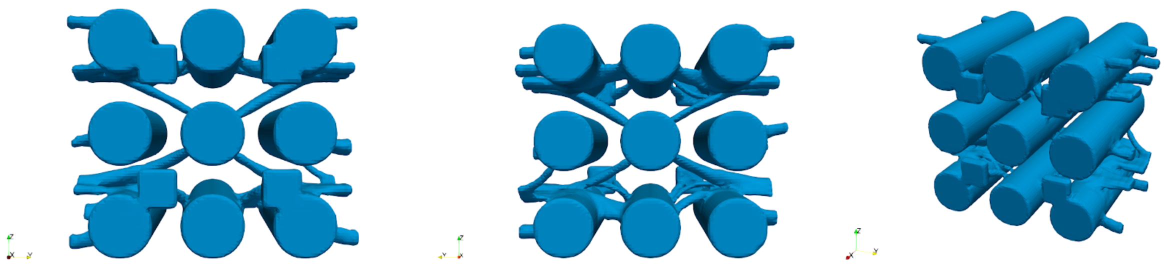

**(a) Front view** **(b) Rear view** **(c) Isometric view**

**Fig. 17 Different views of thermo-mechanically topology-optimized battery pack of iteration 1**

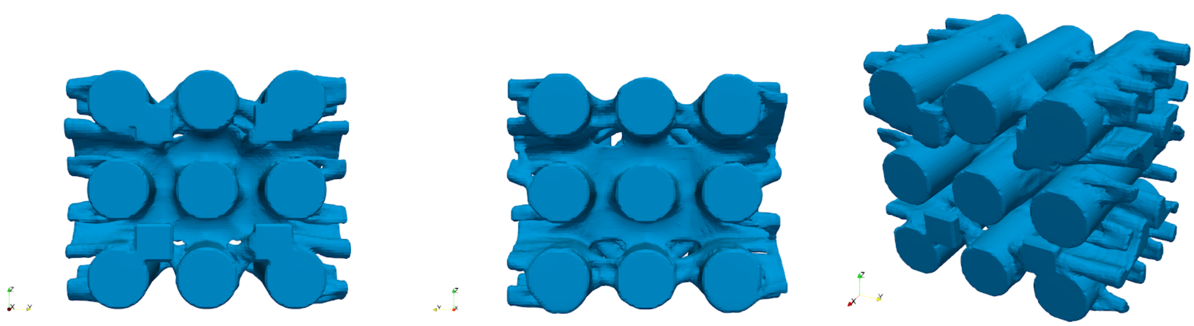

**(a) Front view** **(b) Rear view** **(c) Isometric view**

**Fig. 18 Different views of thermo-mechanically topology-optimized battery pack of iteration 2**

Figure 20a displays the battery pack mass that we obtain as a result of the cell chemistry and battery pack optimization models. The total pack mass is broken up into three parts: First, the mass of the battery cells that are needed to fulfill the battery capacity as modeled by the system-level optimization, which includes 80% depth of discharge limit and 10% mission energy reserve. Second, the mass of the extra cells that need to be added to the battery pack in order to be able to output the mission power profile without cell failure. Third, the battery packaging mass, based on the packaging overhead factor. We see that the packaging overhead increases significantly from iteration to iteration, due to the reasons outlined above. The mission energy demand seems to stabilize after iteration 2, but because of the increase in peak power in iteration 3 more cells still have to be added to guarantee the feasibility of completing the design mission with our selected battery chemistry. Figure 20b shows the consequence of the added cell mass due to power demands and the packaging overhead due to large thermal loads: The effective pack-level energy density decreases significantly compared to the assumed baseline value of 400 $Wh/kg$. This shows the importance of limiting peak power draws and managing cell heat production.

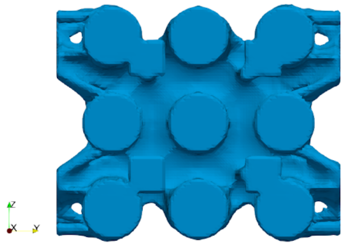


(a) Front view

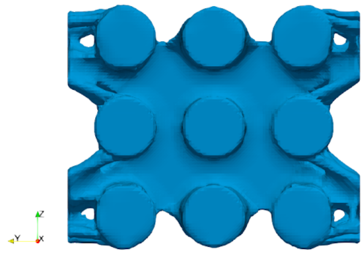

(b) Rear view

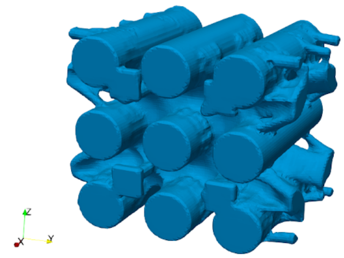

(c) Isometric view

**Fig. 19 Different views of thermo-mechanically topology-optimized battery pack of iteration 3**

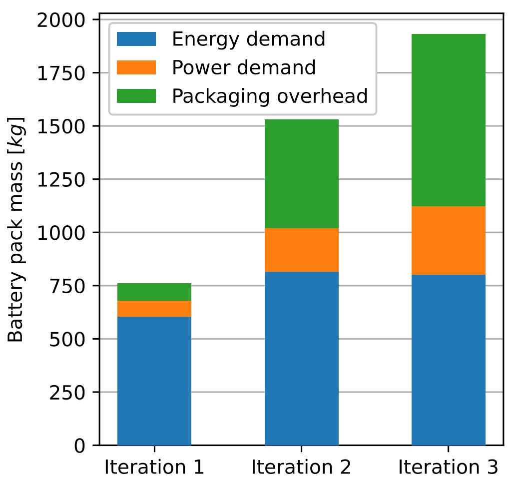


**(a) Battery pack mass, broken up into segments**

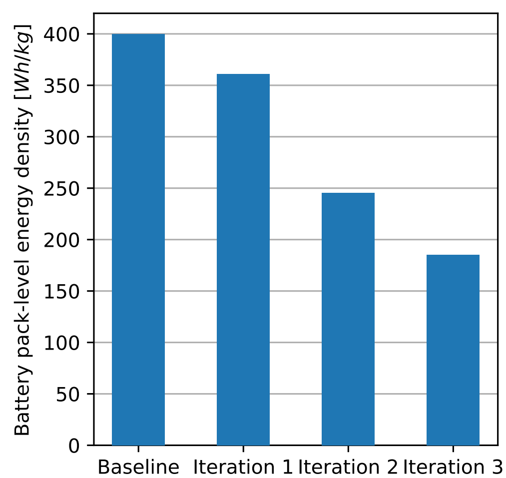


**(b) Effective battery pack-level energy density**

**Fig. 20 Battery pack mass breakdown and resulting effective pack-level energy density per run of the battery optimization**



*4. Wing Structural Design*

Next we look at the last of the subsystem optimizations. Figure 21 shows the optimized wing skin thicknesses in stations along the top and bottom wing surfaces for each iteration. Since the wing aspect ratio and surface area changes little from iteration to iteration, the optimized designs are similar as well. The primary differences are twofold. First, the skin thickness near the the top surface of the wing root decreases from iteration 1 to iteration 2, which brings down the wing mass from 467.42 $kg$ to 450.40 $kg$. Second, the wing surface area and wing span decrease slightly between iteration 2 and iteration 3, which reduces wing mass further to 438.92 $kg$. The panel-wise buckling constraints were active on all skin panels.

## E. Design Parameter Consistency

Lastly we look at the consistency of the design parameters and mass of the wing structure, compared between the system-level and aero-structural optimizations. Figure 22a shows for each iteration the 2-norm of the difference between the (shared) wing thicknesses computed by both the system-level and aero-structural optimizations, as a fraction of the 2-norm of the system-level thickness vector. As can be seen the inconsistency is initially close to 30% and is gradually reduced to only 7% in the third iteration. A similar trend is visible when comparing the wing structural mass predictions of both optimizations, shown in figure 22b. The wing mass in the system-level optimization gradually converges to that of the high-fidelity aero-structural optimization. These results show that our ATC implementation seems successful at

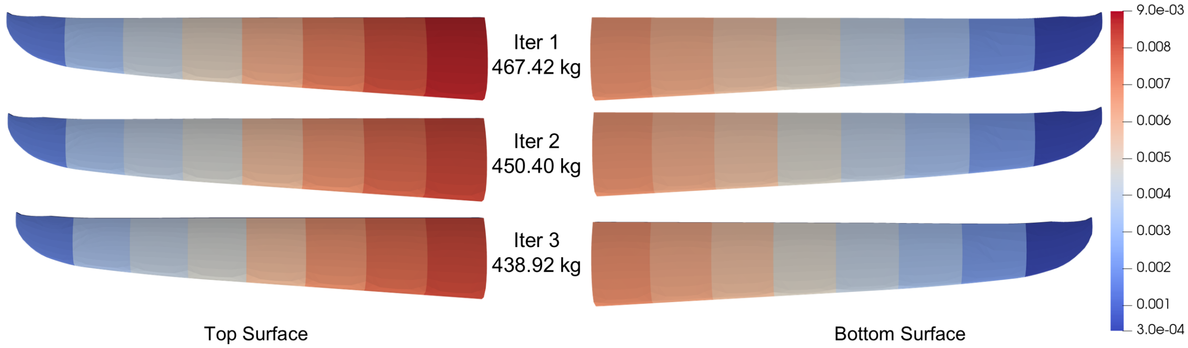


**Fig. 21 Optimized wing surface thicknesses per iteration, thickness *t* given in meters**

achieving consistency between both optimizations.

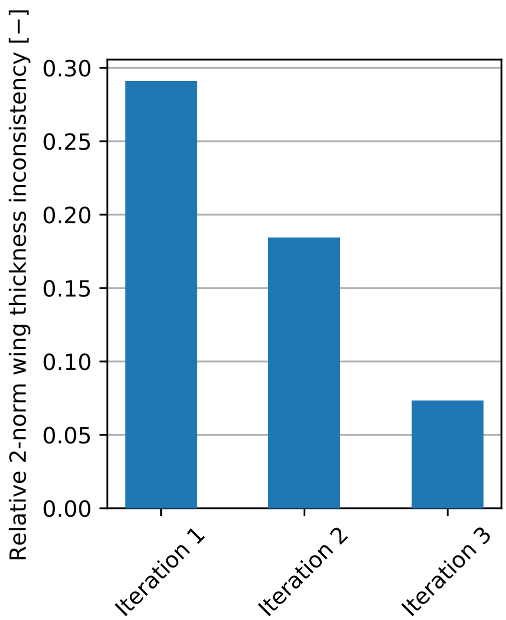


**(a) 2-norm of wing thickness inconsistency per iteration, normalized with 2-norm of wing thickness variable vector**

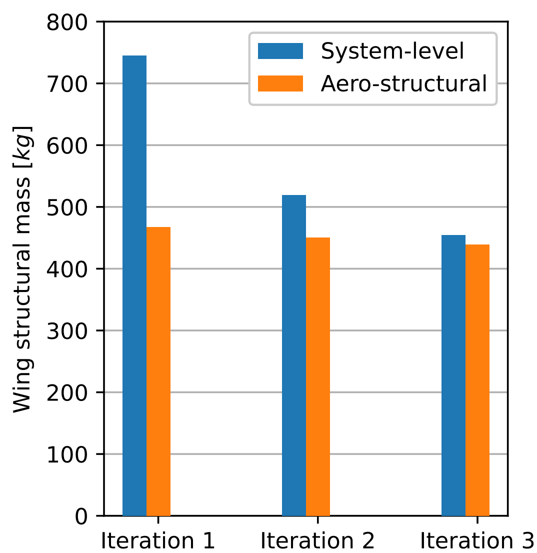


**(b) Wing structural mass as computed by system-level and aero-structural optimizations**

**Fig. 22 Wing thickness inconsistencies and structural mass predictions**

## VI. Conclusions

In this work we carried out distributed Multidisciplinary Design Optimization (MDO) of NASA's Lift + Cruise eVTOL concept vehicle. We coupled a mid-fidelity physics-based system-level optimization that is very similar to the one presented by Ruh et al. [15] to four higher-fidelity sub-optimization models of various systems and design aspects. Our aim is to expand the scope of the system-level optimization. These sub-optimizations consist of the transition trajectory between hover and climb mission segments, the powertrain electronics, battery pack (split into cell-level and pack-level models) and aero-structural wing design. Relevant information, such as the mission power profile and vehicle mass breakdown, is passed from the system-level optimization to each subsystem optimization, after which the sub-optimizations feed back updated optimized subsystem design information to the system-level optimization. The design variables that are shared by the aero-structural and system-level optimizations are made consistent through an Analytical Target Cascading-like distributed MDO architecture.

With our current choice of high energy density battery cell chemistry, extra cells need to be added to the battery pack in order to handle the high discharge rates that are imposed by the hover and transition mission segments. This lowers the effective battery energy density for our design mission and leads to high thermal loads in the battery pack. The result is a battery pack that completes our design mission without reaching our 80% depth of discharge constraint. In order to dissipate the thermal loads we require significant battery packaging mass, further lowering the effective battery energy density. As a consequence of this the gross vehicle mass estimate grows by 37% relative to the initial system-level vehicle optimization. In future work the battery pack temperature limits can likely be increased without jeopardizing the safety of the battery cells. This will also increase the resulting pack-level energy density.

While the optimized efficiencies of the powertrain did not change significantly between outer loop iterations, the high-fidelity aero-structural wing optimization model resulted in a lighter wing structure by expanding the feasible design space and improving the wing structural mass estimate of the system-level box beam model. While the transition trajectory optimization did not directly produce vehicle mass estimations, its results directly affected the system-level optimization. Even though we encountered significant power demand peaks during the transition maneuvers, these follow similar trends as the power demand in hover. This indicates that the source for the large power demand lies in the efficiency of the lift rotors. We found that noise constraints have a significant effect on the efficiency of the lift rotor blades. The resulting increase in power demand has significantly increased the battery pack mass.

Over the course of carrying out the research for this study, we found that the importance of battery cell energy density for winged eVTOL vehicles grows as the design cruise range becomes longer and more energy is required to complete the design mission. For shorter missions, cell power density instead drives battery cell mass, since having fewer available battery cells (owing to lower energy requirements) drives up the resulting cell discharge rates during high-power mission segments. In this work cell power density directly drives vehicle design. The battery pack has leftover capacity at the end of the current design mission, as a result increasing the cruise range by 50% results in an increase in battery pack mass of only 2.6%. When using commercially available cells this suggests that the optimal battery pack for a given mission should combine cells that have high power densities and those with high energy densities, depending on power and energy needs. Stahl et al. [81] considered various battery layouts with this approach for small unmanned aircraft.

We also found that noise constraints had a significant effect on rotor design. Limiting the rotor tip speeds (and thus rotor diameters) resulted in high rotor disk loading during hover and the initial phase of the hover-climb transition maneuver, as well as less efficient rotor blade designs. The net result of this has been an increase in required battery power, which further amplifies the relevance of taking into account battery power density. One solution to mitigate this effect consists of increasing the number of rotors in order to lower the disk loading without increasing rotor diameter. The design payload mass of the lift plus cruise vehicle considered here is more than double that of existing eVTOL vehicles; the resulting high disk loading amplifies the impact of the aforementioned noise constraints.

Lastly, we recommend that battery pack power density be explicitly taken into account for initial sizing and MDO of eVTOL vehicles. While many works emphasize the importance of high battery energy density, only few take into account the effect of the power density on battery mass. Of those works that do, most seem to assume high limits for cell discharge rates along with similar energy densities. In reality, cell power density and energy density need to be traded off in favor of one another: High energy density cells tend to have poor discharge rate limits, while cells with high allowable discharge rates deplete quickly. This relation is visible in taxonomies of battery cell chemistries, commonly referred to as so-called 'Ragone plots' [82]. We found with the approach taken in this work, that power density is a critical factor for the design problem considered here.

## Acknowledgments

The material presented in this paper is supported by NASA under award No. 80NSSC21M0070.

## References

[1] Roskam, J., *Airplane Design*, DARcorporation, Lawrence, Kansas, 1997.

[2] Raymer, D., *Aircraft Design: A Conceptual Approach*, sixth ed., American Institute of Aeronautics and Astronautics, 2018.

[3] Torenbeek, E., *Synthesis of Subsonic Airplane Design*, Springer Dordrecht, 1982.

[4] Hirschberg, M., "Press Release: Vertical Flight Society Electric VTOL Directory Hits 1,000 Designs," , 2024. URL `https://evtol.news/news/press-release-vertical-flight-society-electric-vtol-directory-hits-1000-designs`, accessed on 2024/05/20.

[5] Johnson, W., and Silva, C., "NASA concept vehicles and the engineering of advanced air mobility aircraft," *The Aeronautical Journal*, Vol. 126, No. 1295, 2022, p. 59–91. https://doi.org/10.1017/aer.2021.92.

[6] Palaia, G., Abu Salem, K., Cipolla, V., Binante, V., and Zanetti, D., "A Conceptual Design Methodology for e-VTOL Aircraft for Urban Air Mobility," *Applied Sciences*, Vol. 11, No. 22, 2021. https://doi.org/10.3390/app112210815.

[7] Ugwueze, O., Statheros, T., Horri, N., Bromfield, M. A., and Simo, J., "An Efficient and Robust Sizing Method for eVTOL Aircraft Configurations in Conceptual Design," *Aerospace*, Vol. 10, No. 3, 2023. https://doi.org/10.3390/aerospace10030311.

[8] Brown, A., and Harris, W. L., "Vehicle Design and Optimization Model for Urban Air Mobility," *Journal of Aircraft*, Vol. 57, No. 6, 2020, pp. 1003–1013. https://doi.org/10.2514/1.C035756.

[9] Bhandari, R., Aman Mishra, A., and Chakraborty, I., "Optimization of Lift-Plus-Cruise Vertical Take-Off and Landing Aircraft with Electrified Propulsion," *Journal of Aircraft*, Vol. 61, No. 2, 2024, pp. 392–414. https://doi.org/10.2514/1.C037343.

[10] Pacini, B., Yildirim, A., Davoudi, B., Martins, J. R., and Duraisamy, K., "Towards Efficient Aerodynamic and Aeroacoustic Optimization for Urban Air Mobility Vehicle Design," *AIAA AVIATION 2021 FORUM*, 2021. https://doi.org/10.2514/6.2021-3026.

[11] Pereira, L. T. L., Wang, S., and Ragni, D., "A Preliminary Design Framework for Performance and Noise Assessment of Urban Air Mobility Vehicles," *30th AIAA/CEAS Aeroacoustics Conference (2024)*, 2024. https://doi.org/10.2514/6.2024-3334.

[12] Clarke, M. A., and Alonso, J., "Evaluating the Performance and Acoustic Footprint of Aircraft for Regional and Urban Air Mobility," *AIAA AVIATION 2021 FORUM*, 2021. https://doi.org/10.2514/6.2021-3205.

[13] Silva, C., Johnson, W. R., Solis, E., Patterson, M. D., and Antcliff, K. R., "VTOL Urban Air Mobility Concept Vehicles for Technology Development," *2018 Aviation Technology, Integration, and Operations Conference*, 2018. https://doi.org/10.2514/6.2018-3847.

[14] Sarojini, D., Ruh, M. L., Joshy, A. J., Yan, J., Ivanov, A. K., Scotzniovsky, L., Fletcher, A. H., Orndorff, N. C., Sperry, M., Gandarillas, V. E., Asher, I., Chambers, J. T., Gill, H., Lee, S., Cheng, Z., Rodriguez, G., Zhao, S., Mi, C., Nascenzi, T., Cuatt, T., Winter, T. F., Guibert, A. T., Cronk, A., Kim, H. A., Meng, S., and Hwang, J. T., "Large-Scale Multidisciplinary Design Optimization of an eVTOL Aircraft using Comprehensive Analysis," *AIAA SCITECH 2023 Forum*, 2023. https://doi.org/10.2514/6.2023-0146.

[15] Ruh, M. L., Fletcher, A., Sarojini, D., Sperry, M., Yan, J., Scotzniovsky, L., van Schie, S. P., Warner, M., Orndorff, N. C., Xiang, R., Joshy, A. J., Zhao, H., Krokowski, J., Gill, H., Lee, S., Cheng, Z., Cao, Z., Mi, C., Silva, C., Wolfe, L., Chen, J.-S., and Hwang, J. T., "Large-scale multidisciplinary design optimization of a NASA air taxi concept using a comprehensive physics-based system model," *AIAA SCITECH 2024 Forum*, 2024. https://doi.org/10.2514/6.2024-0771.

[16] Kim, H. M., Michelena, N. F., Papalambros, P. Y., and Jiang, T., "Target Cascading in Optimal System Design ," *Journal of Mechanical Design*, Vol. 125, No. 3, 2003, pp. 474–480. https://doi.org/10.1115/1.1582501.

[17] Tosserams, S., Kokkolaras, M., Etman, L. F. P., and Rooda, J. E., "A Nonhierarchical Formulation of Analytical Target Cascading," *Journal of Mechanical Design*, Vol. 132, No. 5, 2010, p. 051002. https://doi.org/10.1115/1.4001346.

[18] Sarojini, D., Ruh, M., Yan, J., Scotzniovsky, L., Orndorff, N. C., Xiang, R., Zhao, H., Krokowski, J., Warner, M., van Schie, S., Cronk, A., Guibert, A. T., Chambers, J. T., Wolfe, L., Doring, R., Despins, R., Joseph, C., Anderson, R., Ning, A., Gill, H., Lee, S., Cheng, Z., Cao, Z., Mi, C., Meng, Y. S., Silva, C., Chen, J.-S., Kim, A. A., and Hwang, J. T., "Review of Computational Models for Large-Scale MDAO of Urban Air Mobility Concepts," *AIAA SCITECH 2024 Forum*, 2024. https://doi.org/10.2514/6.2024-0377.

[19] Lowson, M. V., and Ollerhead, J. B., "A Theoretical Study of Helicopter Rotor Noise," *Journal of Sound Vibration*, Vol. 9, No. 2, 1969, pp. 197–222. https://doi.org/10.1016/0022-460X(69)90028-5.

[20] Farassat, F., "Derivation of Formulations 1 and 1A of Farassat," Tech. Rep. NASA/TM-2007–214853, NASA Langley Research Center, 2007.

[21] Ffowcs Williams, J. E., and Hawkings, D. L., "Sound Generated by Turbulence and Surfaces in Arbitrary Motion," *Philosophical Transactions of the Royal Society*, Vol. A264, No. 1151, 1969, pp. 321–342.

[22] Jia, Z., and Lee, S., "Computational Study on Noise of Urban Air Mobility Quadrotor Aircraft," *Journal of American Helicopter Society*, Vol. 67, No. 1, January, 2022, pp. 1–15. https://doi.org/10.4050/JAHS.67.012009.

[23] Jia, Z., and Lee, S., "High-Fidelity Computational Analysis on the Noise of a Side-by-Side Hybrid VTOL Aircraft," *Journal of American Helicopter Society*, Vol. 67, No. 2, April, 2022, pp. 1–14. https://doi.org/10.4050/JAHS.67.022005.

[24] Sagaga, J., and Lee, S., "Performance, Aerodynamics, and Aeroacoustics of Side-by-Side Rotors Using High-Fidelity Computational Fluid Dynamics," *AIAA Journal*, Vol. 61, No. 12, 2023, pp. 5429–5445. https://doi.org/10.2514/1.J062955.

[25] Sagaga, J., and Lee, S., "High-Fidelity Computational Study of Aerodynamic Noise of Side-by-Side Rotor in Full Configuration," *Journal of Sound and Vibration*, Vol. 592, 2024, p. 118607. https://doi.org/10.1016/j.jsv.2024.118607.

[26] Gill, H., and Lee, S., "Development of a New Empirical Rotor Broadband Noise Prediction Models for Urban Air Mobility Applications," *AIAA SciTech Forum*, AIAA Paper 2024–2473, Jan. 2024. https://doi.org/10.2514/6.2024-2473.

[27] Brooks, T. F., Pope, D. S., and Marcolini, M. A., "Airfoil Self-Noise and Prediction," Reference Publication 1218, NASA, 1989.

[28] Amiet, R. K., "Acoustic Radiation from an Airfoil in a Turbulent Stream," *Journal of Sound and Vibration*, Vol. 41, No. 4, 1975, pp. 407–420. https://doi.org/10.1016/S0022-460X(75)80105-2.

[29] Lee, S., Ayton, L., Bertagnolio, F., Moreau, S., Chong, T. P., and Joseph, P., "Turbulent Boundary Layer Trailing-Edge Noise: Theory, Computation, Experiment, and Application," *Progress in Aerospace Sciences*, Vol. 126, 2021, p. 100737. https://doi.org/10.1016/j.paerosci.2021.100737.

[30] Pegg, R. J., "A Summary and Evaluation of Semi-Empirical Methods for the Prediction of Helicopter Rotor Noise," Tech. Rep. NASA–TM–80200, NASA, December 1979.

[31] Schlegel, R., King, R., and Mull, H., "Helicopter Rotor Noise Generation and Propagation," Tech. Rep. USAAVLABS–TR–66–4, U.S. Army Aviation Materiel Laboratories, October 1966.

[32] Lee, S., and Shum, J. G., "Prediction of Airfoil Trailing-Edge Noise Using Empirical Wall Pressure Spectrum Models," *AIAA Journal*, Vol. 57, No. 3, 2019, pp. 888–897. https://doi.org/10.2514/1.J057787.

[33] Li, S., and Lee, S., "Predictions and Validations of Small-Scale Rotor Noise Using UCD-QuietFly," *VFS Aeromechanics for Advanced Vertical Flight Technical Meeting*, San Jose, CA, 2022.

[34] Li, S., and Lee, S., "Prediction of Urban Air Mobility Multi-Rotor VTOL Broadband Noise Using UCD-QuietFly," *Journal of the American Helicopter Society*, Vol. 66, No. 3, Feb. 2021, pp. 1–13. https://doi.org/10.4050/JAHS.66.032004.

[35] Li, S., and Lee, S., "Prediction of Rotorcraft Broadband Trailing-Edge Noise and Parameter Sensitivity Study," *Journal of the American Helicopter Society*, Vol. 65, No. 4, 2020, pp. 1–14. https://doi.org/10.4050/JAHS.65.042006.

[36] Marques, M., Goubev, V. V., Lyrintzis, A. S., and Afari, S. O., "Analysis of e-VTOL Rotor Noise Predictions," *AIAA SciTech Forum*, AIAA Paper 2024–2809, Jan. 2024. https://doi.org/10.2514/6.2024-2809.

[37] Lee, S., "Empirical Wall-Pressure Spectral Modeling for Zero and Adverse Pressure Gradient Flows," *AIAA Journal*, Vol. 56, No. 5, 2018, pp. 1818–1829. https://doi.org/10.2514/1.J056528.

[38] Gandarillas, V., Joshy, A. J., Sperry, M. Z., Ivanov, A. K., and Hwang, J. T., "A graph-based methodology for constructing computational models that automates adjoint-based sensitivity analysis," *Structural and Multidisciplinary Optimization*, Vol. 67, No. 76, 2024. https://doi.org/10.1007/s00158-024-03792-0.

[39] Zanotti, A., Velo, A., Pepe, C., Savino, A., Grassi, D., and Riccobene, L., "Aerodynamic interaction between tandem propellers in eVTOL transition flight configurations," *Aerospace Science and Technology*, 2024, p. 109017.

[40] Reddinger, J.-P., McIntosh, K., Zhao, D., and Mishra, S., "Modeling and trajectory control of a transitioning quadrotor biplane tailsitter," *Vertical Flight Society 75th Annual Forum*, Vol. 93, 2019, pp. 1–10.

[41] Shahjahan, S., Gong, A., Moore, A., and Verstraete, D., "Optimisation of proprotors for tilt-wing eVTOL aircraft," *Aerospace Science and Technology*, Vol. 144, 2024, p. 108835.

[42] Chauhan, S. S., and Martins, J. R., "Tilt-wing eVTOL takeoff trajectory optimization," *Journal of aircraft*, Vol. 57, No. 1, 2020, pp. 93–112.

[43] Qing, L., Juanxia, L., Xingyu, Z., and Juhong, L., "Research of Transition Corridor and Optimal Trajectory for Front-Tilt-Quadplane eVTOL Aircraft," *2023 6th International Conference on Electronics Technology (ICET)*, IEEE, 2023, pp. 898–902.

[44] Droandi, G., Syal, M., and Bower, G., "Tiltwing Multi-Rotor Aerodynamic Modeling in Hover, Transition and Cruise Flight Conditions," *74th Forum of the American Helicopter Society*, 2018, p. 16. URL https://vtol.org/store/product/tiltwing-multirotor-aerodynamic-modeling-in-hover-transition-and-cruise-flight-conditions-12674.cfm.

[45] Hyun, J., Jang, M., Nguyen, T. A., and Lee, J.-W., "Transition Control Planning and Optimization for a Boxed-wing eVTOL Tiltrotor Vehicle using Trim Analysis," *2023 International Conference on Unmanned Aircraft Systems (ICUAS)*, IEEE, 2023, pp. 1128–1135.

[46] Qu, S., Zhu, G., Su, W., and Swei, S. S.-M., "LPV Model-based Adaptive MPC of an eVTOL Aircraft During Tilt Transition Subject to Motor Failure," *International Journal of Control, Automation and Systems*, Vol. 21, No. 2, 2023, pp. 339–349.

[47] Thompson, D., "Robust Control of an Evtol through Transition with a Gain Scheduling LQR Controller," Master's thesis, University of Maryland, College Park, 2020.

[48] Kai, J.-M., "Full-Envelope Flight Control and a Transition Strategy for Compound eVTOL aircrafts," *arXiv preprint arXiv:2312.09629*, 2023.

[49] Lu, Z., Li, H., He, R., and Holzapfel, F., "Energy-Efficient Incremental Control Allocation for Transition Flight via Quadratic Programming," *International Conference on Guidance, Navigation and Control*, Springer, 2022, pp. 4940–4951.

[50] Zhang, X., Bowman, C. L., O'Connell, T. C., and Haran, K. S., "Large electric machines for aircraft electric propulsion," *IET Electric Power Applications*, Vol. 12, No. 6, 2018, pp. 767–779. https://doi.org/10.1049/iet-epa.2017.0639.

[51] Erickson, R. W., and Maksimovic, D., *Fundamentals of power electronics*, 2$^{\text{nd}}$ ed., Springer Science & Business Media, 2007.

[52] Clarke, S., Redifer, M., Papathakis, K., Samuel, A., and Foster, T., "X-57 power and command system design," *2017 IEEE Transportation Electrification Conference and Expo (ITEC)*, IEEE, 2017, pp. 393–400.

[53] Menzi, D., Imperiali, L., Bürgisser, E., Ulmer, M., Huber, J., and Kolar, J. W., "Ultra-Lightweight High-Efficiency Buck-Boost DC-DC Converters for Future eVTOL Aircraft with Hybrid Power Supply," *IEEE Transactions on Transportation Electrification*, 2024. https://doi.org/10.1109/TTE.2024.3375026.

[54] Nawawi, A., Tong, C. F., Yin, S., Sakanova, A., Liu, Y., Liu, Y., Kai, M., See, K. Y., Tseng, K.-J., Simanjorang, R., Gajanayake, C. J., and Gupta, A. K., "Design and Demonstration of High Power Density Inverter for Aircraft Applications," *IEEE Transactions on Industry Applications*, Vol. 53, No. 2, 2017, pp. 1168–1176. https://doi.org/10.1109/TIA.2016.2623282.

[55] Li, J., Abdallah, T., and Sullivan, C. R., "Improved calculation of core loss with nonsinusoidal waveforms," *Conference Record of the 2001 IEEE Industry Applications Conference. 36th IAS Annual Meeting (Cat. No. 01CH37248)*, Vol. 4, IEEE, 2001, pp. 2203–2210.

[56] Mühlethaler, J., "Modeling and multi-objective optimization of inductive power components," Ph.D. thesis, ETH Zurich, 2012.

[57] Gammeter, C., Krismer, F., and Kolar, J. W., "Weight Optimization of a Cooling System Composed of Fan and Extruded-Fin Heat Sink," *IEEE Transactions on Industry Applications*, Vol. 51, No. 1, 2015, pp. 509–520. https://doi.org/10.1109/TIA.2014.2336977.

[58] Wang, P., McCluskey, P., and Bar-Cohen, A., "Two-Phase Liquid Cooling for Thermal Management of IGBT Power Electronic Module," *Journal of Electronic Packaging*, Vol. 135, No. 2, 2013, p. 021001. https://doi.org/10.1115/1.4023215.

[59] Zou, J., Brooks, N. C., Coday, S., Ellis, N. M., and Pilawa-Podgurski, R. C., "On the size and weight of passive components: Scaling trends for high-density power converter designs," *2022 IEEE 23rd Workshop on Control and Modeling for Power Electronics (COMPEL)*, IEEE, 2022, pp. 1–7.

[60] Planella, F. B., Sheikh, M., and Widanage, W. D., "Systematic derivation and validation of a reduced thermal-electrochemical model for lithium-ion batteries using asymptotic methods," *Electrochimica Acta*, Vol. 388, 2021, p. 138524.

[61] Marquis, S. G., Sulzer, V., Timms, R., Please, C. P., and Chapman, S. J., "An asymptotic derivation of a single particle model with electrolyte," *Journal of The Electrochemical Society*, Vol. 166, No. 15, 2019, p. A3693.

[62] Doyle, M., Fuller, T. F., and Newman, J., “Modeling of galvanostatic charge and discharge of the lithium/polymer/insertion cell,” *Journal of the Electrochemical society*, Vol. 140, No. 6, 1993, p. 1526.

[63] Sulzer, V., Marquis, S. G., Timms, R., Robinson, M., and Chapman, S. J., “Python battery mathematical modelling (PyBaMM),” *Journal of Open Research Software*, Vol. 9, No. 1, 2021.

[64] Chen, C.-H., Planella, F. B., O’Regan, K., Gastol, D., Widanage, W. D., and Kendrick, E., “Development of Experimental Techniques for Parameterization of Multi-scale Lithium-ion Battery Models,” *Journal of The Electrochemical Society*, Vol. 167, No. 8, 2020, p. 080534. https://doi.org/10.1149/1945-7111/ab9050.

[65] Guibert, A. T., Bookwala, M., Cronk, A., Meng, Y. S., and Kim, A. A., “Thermo-Mechanical Level-Set Topology Optimization of an eVTOL Battery Pack,” *AIAA SCITECH 2024 Forum*, 2024, p. 2362.

[66] Alnæs, M., Blechta, J., Hake, J., Johansson, A., Kehlet, B., Logg, A., Richardson, C., Ring, J., Rognes, M. E., and Wells, G. N., “The FEniCS project version 1.5,” *Archive of numerical software*, Vol. 3, No. 100, 2015.

[67] Jauregui, C. M., Hyun, J., Neofytou, A., Gray, J. S., and Kim, H. A., “Avoiding reinventing the wheel: reusable open-source topology optimization software,” *Structural and Multidisciplinary Optimization*, Vol. 66, No. 6, 2023, p. 145.

[68] Schie, S. P. C. V., Zhao, H., Yan, J., Xiang, R., Hwang, J. T., and Kamensky, D., “Solver-Independent Aeroelastic Coupling For Large-Scale Multidisciplinary Design Optimization,” *AIAA SCITECH 2023 Forum*, 2023. https://doi.org/10.2514/6.2023-0727.

[69] Van Schie, S. P. C., Warner, M. A. P., Fletcher, A. H., and Hwang, J. T., “Enforcing Work Conservation in Modular Aeroelastic Coupling For Multidisciplinary Design Optimization,” *AIAA SciTech 2024 Forum*, 2024. https://doi.org/10.2514/6.2024-2411.

[70] Ruh, M. L., Liu, X., Yu, R., and Hwang, J. T., “Airfoil shape parameterization using reconstruction-error-minimizing generative adversarial networks,” *AIAA AVIATION 2023 Forum*, 2023, p. 3722.

[71] Baratta, I. A., Dean, J. P., Dokken, J. S., Habera, M., Hale, J. S., Richardson, C. N., Rognes, M. E., Scroggs, M. W., Sime, N., and Wells, G. N., “DOLFINx: The next generation FEniCS problem solving environment,” , Dec. 2023. https://doi.org/10.5281/zenodo.10447666.

[72] Xiang, R., van Schie, S. P. C., Scotzniovsky, L., Yan, J., Kamensky, D., and Hwang, J. T., “Automating adjoint sensitivity analysis for multidisciplinary models involving partial differential equations,” *Structural and Multidisciplinary Optimization*, Vol. 67, 2024. https://doi.org/10.1007/s00158-024-03847-2.

[73] Warner, M. A. P., Fletcher, A. H., van Schie, S. P. C., and Hwang, J. T., “A Method for Modular MDO Model Assembly via a Solver Independent Field Representation,” *AIAA SciTech 2024 Forum*, 2024.

[74] Young, W. C., and Budynas, R. G., *Roark’s Formulas for Stress & Strain*, seventh ed., McGraw-Hill, 2001.

[75] Martins, J. R. R. A., and Lambe, A. B., “Multidisciplinary Design Optimization: A Survey of Architectures,” *AIAA Journal*, Vol. 51, No. 9, 2013, pp. 2049–2075. https://doi.org/10.2514/1.J051895.

[76] Chinthoju, P., Lee, Y. H., Das, G. K., James, K. A., and Allison, J. T., “Optimal Design of eVTOLs for Urban Mobility using Analytical Target Cascading (ATC),” *AIAA SCITECH 2024 Forum*, 2024. https://doi.org/10.2514/6.2024-2235.

[77] Electric VTOL News, “Joby Aviation S4 (production prototype),” , 2024. URL https://evtol.news/joby-aviation-s4-production-prototype, accessed on 2024/12/05.

[78] Electric VTOL News, “Archer Aviation Midnight (production aircraft),” , 2024. URL https://evtol.news/archer/, accessed on 2024/12/05.

[79] Electric VTOL News, “Wisk Aero Generation 6 (pre-production prototype),” , 2024. URL https://evtol.news/wisk-aero-generation-6, accessed on 2024/12/05.

[80] Yan, J., Sperry, M., Kamensky, D., and Hwang, J. T., “Dynamic topology optimization of battery packs for eVTOL aircraft under time-dependent loading,” *AIAA AVIATION 2021 FORUM*, 2021. https://doi.org/10.2514/6.2021-3068.

[81] Stahl, P., Roessler, C., and Hornung, M., “Modelling and Performance Impact of High Power/High Energy Battery Hybrids on Fixed-Wing eVTOL UAV,” *AIAA Scitech 2020 Forum*, 2020. https://doi.org/10.2514/6.2020-0260.

[82] Beyers, I., Bensmann, A., and Hanke-Rauschenbach, R., “Ragone plots revisited: A review of methodology and application across energy storage technologies,” *Journal of Energy Storage*, Vol. 73, 2023, p. 109097. https://doi.org/10.1016/j.est.2023.109097.